Numerical modelling of column experiments to investigate in-situ bioleaching as an alternative mining technology

Gautier Laurent, Caroline Izart, Bénédicte Lechenard, Fabrice Golfier, Philippe Marion, Pauline Collon, Laurent Truche, Jean-Jacques Royer, Lev Filippov

Author's Preprint – Published in Hydrometallurgy
10.1016/j.hydromet.2019.07.002

Numerical Modelling of Column Experiments to Investigate In-Situ Bioleaching as an Alternative Mining Technology

Gautier Laurent[1,‡,*], Caroline Izart[1], Bénédicte Lechenard[1], Fabrice Golfier[1], Philippe Marion[1], Pauline Collon[1], Laurent Truche[1,§], Jean-Jacques Royer[1], and Lev Filippov[1]

[1]*Université de Lorraine, CNRS, Laboratoire GeoRessources, 54000, Nancy, France*
[*]*Corresponding author: g.laurent.research@gmail.com; gautier.laurent@univ-orleans.fr*
[‡]*Present address: Univ. Orléans, CNRS, BRGM, ISTO, UMR 7327, F–45071, Orléans, France.*
[§]*Present address: Univ. Grenoble Alpes, CNRS, ISTERRE, 38400, Grenoble, France*

Graphical Abstract

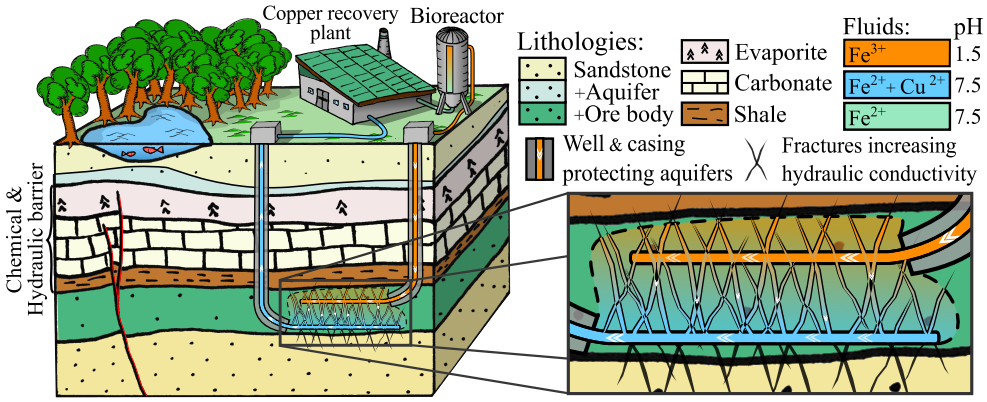

Contents

Author's Preprint – Published in Hydrometallurgy
10.1016/j.hydromet.2019.07.002

Numerical Modelling of Column Experiments to Investigate In-Situ Bioleaching as an Alternative Mining Technology

Gautier Laurent[1,‡,*], Caroline Izart[1], Bénédicte Lechenard[1], Fabrice Golfier[1], Philippe Marion[1], Pauline Collon[1], Laurent Truche[1,§], Jean-Jacques Royer[1], and Lev Filippov[1]

[1]*Université de Lorraine, CNRS, Laboratoire GeoRessources, 54000, Nancy, France*
[*]*Corresponding author: g.laurent.research@gmail.com; gautier.laurent@univ-orleans.fr*
[‡]*Present address: Univ. Orléans, CNRS, BRGM, ISTO, UMR 7327, F–45071, Orléans, France.*
[§]*Present address: Univ. Grenoble Alpes, CNRS, ISTERRE, 38400, Grenoble, France*

Highlights

- An alternative mining process based on indirect in-situ bioleaching is introduced
- The mining process is oriented towards waste and environmental impact minimization
- Combined experimental and numerical models of leaching process are developed
- Dual porosity reactive transport models account for observed retardation effects
- Diffusion through grains of various sizes impacts extraction and transfer rates

Abstract This publication investigates indirect in-situ bioleaching as an alternative mining technology for minimizing waste production, environmental impact, and chemical consumption. The process consists in injecting a leaching solution into a targeted ore body for dissolving base metal bearing minerals, while iron-oxidizing microorganisms regenerate the solution. In this contribution, we present laboratory column experiments that investigate the impact of grain size on the action of an acidic oxidizing solution in contact with ore samples crushed at different grain sizes. These results are used for developing a one-dimensional reactive transport model based on PhreeqC software. In this model, porous and fractured media are approached by a dual porosity reactive transport model where dissolution reactions are described by kinetics. Column experiments are used as a reference for calibrating the key parameters of the numerical models, which include the relative volume of mobile and immobile zones within the dual porosity medium and the exchange rate between these two volumes. This model is then adapted to in-situ conditions by considering the preferential flow of fluids through natural or artificial fractures of enhanced hydraulic conductivity. These models are used to discuss key elements affecting the feasibility of coupling bioleaching and in-situ recovery for improving the sustainability of mining, especially for deep and complex ore deposits.

Keywords
In-Situ Recovery
Bioleaching
Numerical Modelling
Reactive Transport
Dual Porosity
Copper

Introduction

The mineral resource industry faces two opposing demands giving rise to the need to develop alternative approaches to mining [Izatt et al., 2014; Petrie, 2007; Rankin, 2011]. On the one hand, there is a rapid evolution of markets and technologies, with an increasing demand for both strategic and base metals, which comes along with an increasing scarcity of easily exploitable deposits [Moss et al., 2011]. On the other hand, a rightful increasing concern for environmental impact places public acceptance as one of the main challenges to be dealt with when developing new mining projects [Franks et al., 2014; Moffat and Zhang, 2014], especially in relatively densely populated areas such as the European countries. Indeed, mineral resource production represents one of the most influential impacts on the environment, affecting ecology, landscape, and human infrastructures [Kesler and Simon, 2015]. This situation calls for the development of widely applicable production processes that are both efficient and environmentally friendly. Such processes should cause limited impacts on landscape, water resources, and ecosystems, while minimizing waste and dump production [Rankin, 2011].

Over the last decades, academic research and industry have expended considerable efforts on developing such sustainable approaches with, for example, an increasing use of in-situ recovery [Seredkin et al., 2016; Sinclair and Thompson, 2015] and bioleaching [Kutschke et al., 2015; Rawlings, 2002; Rawlings and Johnson, 2007]. The BIOMOre project [Filippov et al., 2017; Matthies et al., 2017] proposes to combine the benefit from these two technologies into an alternative mining process referred to as indirect in-situ bioleaching (Section 1). Within this project, the applicability of this new mining technology is explored through laboratory experiments, numerical modelling, and an in-situ pilot experiment. The Kupferschiefer deposits, for which surface bioleaching has already been proposed [Kutschke et al., 2015], are considered as a case study for investigating the extraction of copper from its mineralised sandstones.

The success of in-situ recovery is highly dependent on the efficiency of the interaction between the leaching solution and the porous medium [Seredkin et al., 2016]. Within the Zechstein sandstones, as for most mineralised sedimentary rocks, the hydraulic conductivity of the porous medium would be a controlling factor. It may have to be increased by

either hydraulic stimulation or blasting, which would generate a complex medium with solid grains and porosities of various sizes. While these hydrodynamic aspects are relatively well controlled during surface processing where the size of rock elements can be optimised for recovery, the limitations introduced by in-situ conditions on the percolation of leaching solutions within rock elements of various sizes requires investigation. In this work, we present an approach that combines laboratory experiments and numerical simulations with the objective of investigating the effect of grain size on the in-situ bioleaching process, and to prepare for future in-situ pilot plants and exploitations. In this framework, the term *grain* is to be considered as a macroscopic notion that refers to millimetric groups of several minerals with an internal porosity (cf. blow-up in Fig. 5A), such as typically produced by crushing rock samples into millimetric particles. It corresponds to particles as described by Fig. 2a in Petersen [2010].

Comparison between experimental data and reactive transport models provides valuable insights into the fluid-rock interactions and expands the analysis of control parameters taking part in such a process. While a relatively complete theoretical framework exists for reactive transport (e.g., [Steefel et al., 2005, 2015; Steefel and Maher, 2009], and references therein), simulations still heavily rely on experimental results for accurately calibrating physical and chemical parameters, such as kinetic rates and hydrodynamic coefficients.

Chemical reaction kinetics are generally assessed by experiments based on finely ground ore samples with sufficiently vigorous agitation to eliminate mass transport effects [Blanc et al., 2012; Bouffard and Dixon, 2001; Habbache et al., 2009], placing them under ideal experimental conditions. Fine-grain experiments are useful for understanding the governing phenomena and reactions of each mineral phase to leaching solution, but such ideal conditions are not practically achievable in-situ, where leaching solution would circulate within fractures or between rock elements with various porosities and sizes.

The series of experiments presented in Section 2 complements the work of Pakostova et al. [2018] by considering different grain size fractions, which provides valuable information on the effect of the architecture and size of the rock medium elements on the leaching process (e.g., final recovery, rate of extraction). This in-situ architecture would relate either to the intrinsic nature of the hosting rock, which can not be directly controlled, or to the applied stimulation process where required (fracking or blasting). Either way, the optimisation of the leaching and/or stimulation processes would rely on the precise knowledge of the impact of the resulting architecture of in-situ rock elements on the leaching process.

To this aim, we developed a one-dimensional dual-porosity model that reproduces the experimental observations and enables a better understanding of the chemical and hydrological processes at stake in the leaching process (Section 3). This model is further developed and adapted to in-situ conditions by considering the circulation of the leaching solution through natural or artificial fracture corridors of higher hydraulic conductivity (Section 4). Key elements for a practical application of in-situ bioleaching as a sustainable mining technology are finally discussed based on the proposed numerical models.

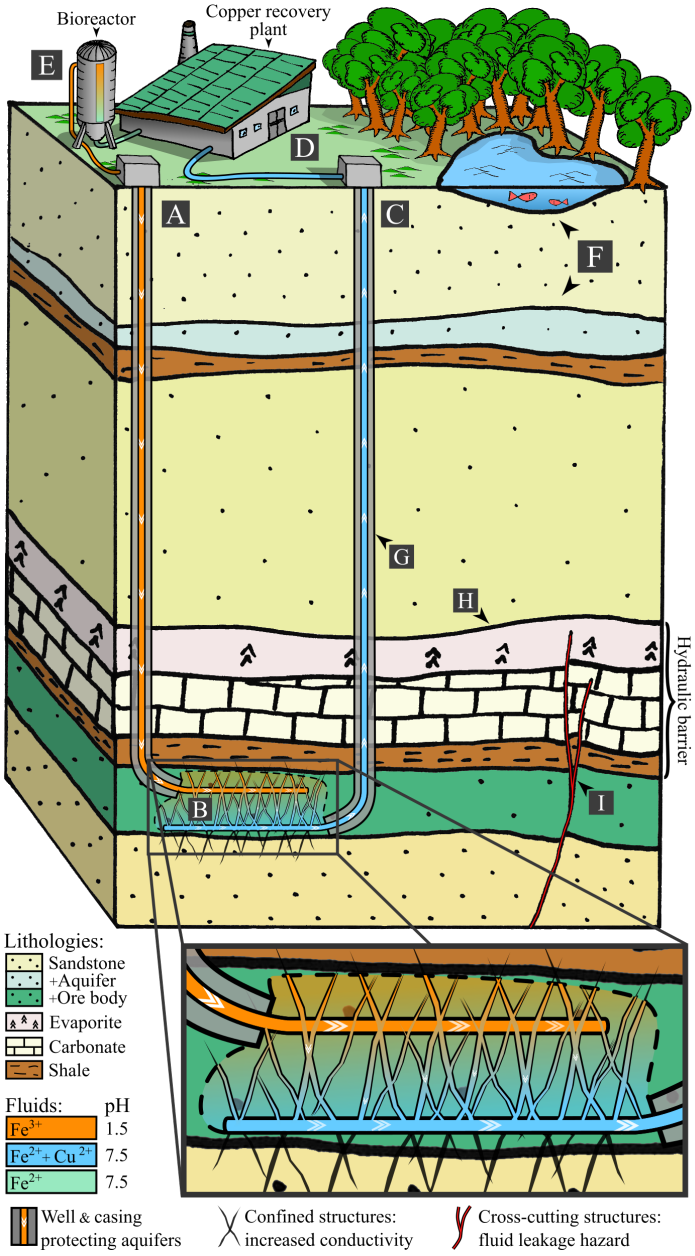

Figure 1 Indirect coupling of in-situ recovery and bioleaching. A: injection of an acidic oxidizing leaching solution. B: percolation through ore deposit and dissolution of target minerals. C: recovery of pregnant leach solution at the surface. D: extraction of metals of interest. E: recycling of the leaching solution thanks to iron-oxidizing microorganisms. The overall process aims at minimizing environmental impact and waste production, but care should be taken for protecting aquifers and environment (F). This can be achieved by ensuring well integrity (G), by taking advantage of natural chemical and hydraulic barrier (H), and by staying away from natural geo-hazards such as faults (I).

1 BIOMOre: an alternative mining technology

The BIOMOre project proposes indirect in-situ bioleaching as an alternative mining technology (Fig. 1). This process takes advantage of both in-situ recovery, for minimizing environmental impact and reducing waste [Seredkin et al., 2016], and biomining, which is recognised as an environmentally friendly and cost limiting alternative to chemical approaches [Rawlings, 2002; Rawlings and Johnson, 2007].

In-situ recovery consists in exploiting an ore body in place by circulating a leaching solution instead of resorting to excavation or galleries. It has been used for over a century for extracting various commodities such as copper [Sulli-

van, 1931], and has become one of the principal extraction method for uranium in the last decades [Bhargava et al., 2015; Seredkin et al., 2016]. Leaching is commonly applied on the surface in tanks or heaps [Sullivan, 1931; Riekkola-Vanhanen, 2013; Wang, 2005], but is more interestingly applied in-situ when geological settings are favourable. Even if uranium remains the most common commodity mined by in-situ recovery, this technique has recently received a growing interest for a wide range of other metals, e.g., gold [Martens et al., 2012], and could bring a similar technological breakthrough as it triggered for uranium in the beginning of the twenty-first century [Seredkin et al., 2016]. In addition to its potential for reducing Capital Expenditures (CapEx) for infrastructure and mine development, in-situ recovery represents a formidable avenue for reducing environmental impact and needs for remediation. It dramatically reduces landscape alteration, excavation, and aquifer dewatering, while yielding less waste and tailing dumps as compared to open pit and underground mining.

As a complement to in-situ recovery, biotechnologies provide interesting solutions for further limiting environmental impact as well as reducing Operational Expenditures (OpEx). The use of microbes for mining has a long history. They have been used since antiquity for mining metals such as copper at the Rio Tinto mine in Spain [Rawlings, 2002]. Even if the microbial activity was not understood at that time, biotechnologies have since then been intensively investigated [Dresher, 2004; Lundgren and Silver, 1980; Harrison and Arthur, 1984; Rawlings, 2002; Rawlings and Johnson, 2007; Rawlings and Silver, 1995; Rohwerder et al., 2003]. In most cases, biomining appears to be more environmentally friendly than roasting or smelting – in particular, it uses less energy, chemicals, and avoids producing various environmentally harmful chemical products [Rawlings, 2002; Pakostova et al., 2018]. Bioleaching is usually applied at the surface in heaps or stirred tanks [Rawlings, 2002; Rawlings and Silver, 1995; Riekkola-Vanhanen, 2013; Wang, 2005].

In existing bioleaching processes, microorganisms are directly mixed together with either the ore or the concentrates [Rawlings, 2002], but this approach would bring technical issues in the case of in-situ recovery. Injecting microorganisms into the deposit would make it difficult to ensure optimal conditions for their development. In addition, it would require solutions for limiting their dissemination and for mining remediation. The proposed process thus implies to decouple the dissolution of minerals (Fig. 1B) from the regeneration of the leaching solution (Fig. 1E), as demonstrated in Pakostova et al. [2018]. It exploits the indirect leaching capabilities of certain microorganisms to remotely dissolve sulphide minerals by mediation of the oxidation-reduction reactions of iron [Lundgren and Silver, 1980; Rawlings, 2002; Tributsch, 2001]. In the proposed process, the microorganisms are contained at the surface in a bioreactor [Abhislash et al., 2012], which continuously regenerates a leaching solution made of sulphuric acid and dissolved iron III. The pH of the solution has to be maintained at very low values for the microorganisms to work properly, and to prevent the precipitation of iron-hydroxides and sulphates [Kutschke et al., 2015].

Ultimately, the process proposed within the BIOMOre project consists in exploiting ore bodies by circulating an acidic oxidizing leaching solution that is regenerated by the action of iron-oxidizing microorganisms [Filippov et al., 2017; Matthies et al., 2017]. Before being regenerated, the pregnant leach solution (i.e., bearing dissolved target metals) is treated hydrometallurgically for extracting any product of interest or any component that would be harmful to the process, such as chlorine [Pakostova et al., 2018].

Although in-situ recovery and biomining are both established technologies, their combination still raises many questions and challenges. For example, leaching solution pathways need to be controlled by managing natural or enhanced hydraulic conductivity and analysing the morphology of deposits. This technology also calls for reliable prediction of recovery and kinetics, which supposes advanced knowledge of minerals in place and fluid-rock interactions. These challenges require growing experience by learning both from existing technologies [Seredkin et al., 2016], and from new experimental and numerical investigations such as presented in this contribution.

2 Experimental column leaching of copper ore

This section presents the main results of several column leaching experiments that were designed for studying the potential efficiency of in-situ bioleaching, and the effect of grain size on the leaching process. To this aim, various grain size fractions have been generated by grinding and sieving the original hard rock samples. The labels used to refer to each grain size fraction are presented in Table 1. This table also presents the average grain size radius that has been used for numerical computations (as in Section 4.1) for each fraction. It corresponds to the radius of a sphere with an average volume considering the minimum and maximum size of each fraction.

The rock samples used in each series originate from the Zechstein sandstones [Oszczepalski, 1999], which characterisation is summarized in Section 2.1. Section 2.2 describes the experimental protocol, and Section 2.3 presents the main observations that are used as a basis for the numerical modelling proposed in Section 3 and 4.

Table 1 Experimental series and grain size fraction.

Series name	C1	C2	C3	C4
Grain size fraction (mm)	< 0.2	0.2 – 1.0	1.0 – 2.0	2.0 – 8.0
Average radius (mm)	0.079	0.398	0.825	3.191

2.1 Qualitative and quantitative characterisation

The ore samples that are used in this study originate from the Rudna mine located North of Polkowilze town in Lower Silesia, Poland. This deposit is hosted within the Kupferschiefer formation, a sedimentary unit with copper, lead, zinc, silver, and platinum group element mineralisation [Oszczepalski, 1999], whose deposition relates to brine circulations [Kucha and Pawlikowski, 1986]. The rock samples belong to the mineralised Zechstein sandstones that underlies the Kupferschiefer black shales. The black shales represent the main mineralisation, but the sandstones have been preferred as they benefit from a higher hydraulic conductivity and a lower carbonate content.

The material for each experimental series has been analysed by various techniques including Scanning Electron

Table 2 Chemical element composition of the different grain size fractions.

Class	Weight		Elements (class mass %)										
	(kg)	(%)	$Cu^{\dagger}$	$Ca^{\dagger}$	$Cl^{\dagger,*}$	$Mg^{\ddagger}$	$Si^{\dagger}$	$Fe^{\dagger}$	$K^{\dagger}$	$Na^{\ddagger}$	$Al^{\star}$	$S(SO_4)^{\ddagger,1}$	$S(S)^2$
C1	4.340	23	1.90	1.64	0.76	0.53	28.56	0.58	1.71	0.42	1.71	0.08	0.60
C2	5.605	29	1.81	0.98	0.51	0.30	32.85	0.55	1.16	0.30	1.50	0.06	0.64
C3	2.598	14	2.40	1.77	0.64	0.52	38.09	0.65	1.45	0.38	1.66	0.08	0.78
C4	6.593	34	2.21	1.70	0.40	0.50	31.06	0.63	1.32	0.36	1.74	0.08	0.85
Global	19.136	100	2.05	1.49	0.54	0.45	31.16	0.60	1.38	0.36	1.65	0.07	0.72

†: measured by portable XRF (NITON) with calibration from ICP-MS measurements (*: unavailable calibration).
‡: measured by Atomic Absorption Spectrometry (AAS); ⋆: measured by laboratory XRF (Brücker).
1: $S(SO_4)$ is the amount of sulphur in sulphates, measured by Atomic Absorption Spectrometry (AAS).
2: S(S) is the amount of sulphur in sulphides, obtained by removing $S(SO_4)$ from the total sulphur measured with XRF.

Table 3 Reconstructed mineral composition of the different grain size fractions.

Class	Recon-structed mass %	Elements (% of the mass of each grain size fraction)											
		Halite $NaCl$	Thenardite Na_2SO_4	Calcite $CaCO_3$	Dolomite $CaMg(CO_3)_2$	Ankerite $CaFe(CO_3)_2$	Atacamite $Cu_2Cl(OH)_3$	Anilite $Cu_{1.75}S$	Bornite Cu_5FeS_4	Pyrite FeS_2	Microcline $KAlSi_3O_8$	Kaolinite $Al_2Si_2O_5(OH)_4$	Quartz SiO_2
C1*	82.67	0.75	1.20	1.46	4.05	0.96	1.82	0.75	0.37	0.64	12.21	7.57	50.90
C2	82.82	0.56	0.25	0.58	2.28	1.38	0.40	1.64	0.47	0.29	8.26	3.33	63.38
C3	85.72	0.69	0.35	1.43	3.94	1.83	0.45	2.22	0.64	0.21	10.31	3.15	60.50
C4	83.01	0.63	0.33	1.54	3.78	1.40	0.34	2.10	0.60	0.42	9.42	3.94	58.51
Global	83.24	0.65	0.51	1.23	3.42	1.35	0.71	1.67	0.52	0.40	9.83	4.48	58.48

Mineral compositions are reconstructed from AAS and XRF measurements (Table 2), c.f. Appendix A.
*: missing experimental information is compensated by optimisation based on XRF and SEM image analysis.

Microscope (SEM) and electron microprobe (EPMA), X-Ray Fluorescence (XRF) spectroscopy, Atomic Absorption Spectrometry (AAS), Inductively Coupled Plasma Mass Spectrometry (ICP-MS), Fourier Transform Infra-Red spectroscopy (FTIR), and X-Ray Computed Tomography (XCT). While each grain size fraction originates from the same original hard rock, they present slight dissimilarities due to the progressive crushing and sieving process. Depending on their relative mechanical strength, some minerals such as halite and atacamite are preferentially found in the finest grain-size fractions. Ideally, each grain size fraction would have been generated from fresh rock samples to limit this effect, but there was not enough material for this approach and each smaller grain size fraction was processed from the residuals of the larger fraction. These discrepancies can be observed from the chemical analyses (Table 2), and mineral reconstructions (Table 3), but the different series exhibit the same overall composition and produce consistent experimental results (Section 2.3).

The SEM images of samples after fresh breakage revealed a complex assemblage of inter-granular minerals within a majority of quartz grains and rare feldspar minerals (Fig. 2). Associated minerals can be subdivided into: (1) calcium, magnesium, and iron carbonates, (2) halogen and sulphate Ca-Na salts, (3) alkaline feldspars, and (4) various copper bearing minerals. For simplification purpose, carbonates are here considered as consisting of three minerals, i.e., calcite, dolomite, and Mg and Mn free ankerite ($CaFe(CO_3)_2$).

Copper is mostly found in sulphide minerals among which bornite and Cu(I)-Cu(II) sulphides. For most copper sulphides, EPMA measurements yield a ratio of copper over sulphur close to 1.7, which also corresponds to the observed global average ratio. In this study, copper sulphides are thus referred to as anilite ($Cu_{1.75}S$), which is the copper sulphide mineral that has the closest corresponding chemical formula. A significant amount of atacamite, a copper chloride hydroxide ($Cu_2Cl(OH)_3$), is also to be noted. It is estimated to account for up to 2 % of rock mass and up

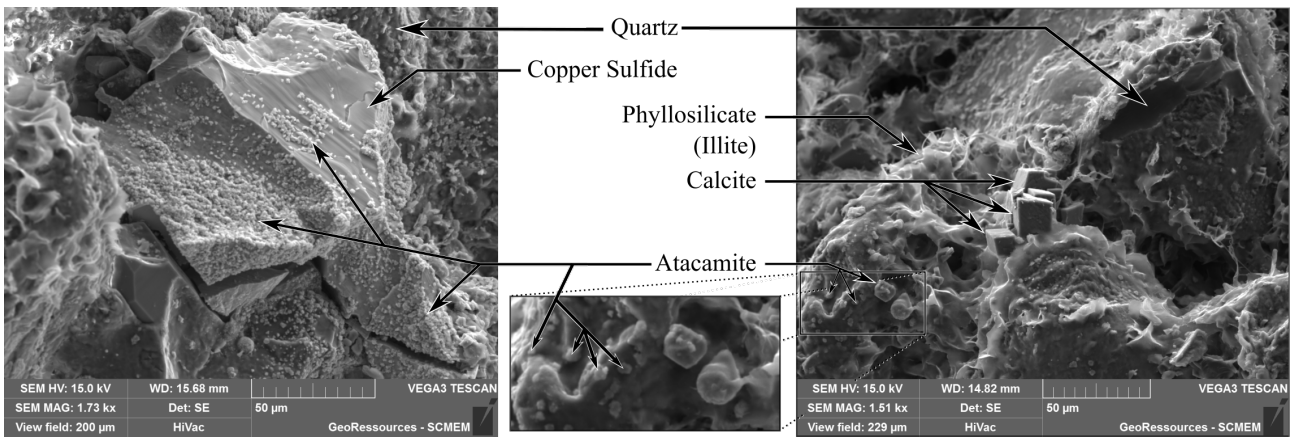

Figure 2 Two secondary electrons SEM images of sample surface after fresh breakage. All phases except quartz and rare feldspars are intergranular fillings.

to 15 % of copper mass. Atacamite is treated with special care for three reasons: (1) it is one of the principal copper bearing minerals in this mineral association, (2) its dissolution yields chlorine, which is detrimental to the processing of the pregnant leach solution, and for the iron-oxidizing microorganisms [Pakostova et al., 2018], and (3) it tends to raise the pH of the leaching solution.

Tomographic analyses confirm the intergranular localisation of sulphides, salts, carbonates, and atacamite. They also provide an estimate of the macro-porosity, which amounts to about 8.5 %. Mercury porosimetry refined this figure to a range from 10 %, for the highly mineralised area, to 14 % within the less mineralised zones.

Table 2 summarizes the concentration of the principal elements found in the different grain size fractions. Most elements were measured by portable X-Ray Fluorescence (Niton™ XL3t GOLDD+) calibrated with respect to ICP-MS measurements. For chlorine, the calibration was not available. Based on the calibration for other elements, we consider that the actual concentration could be up to 20 % lower than that estimated from NITON alone. This uncertainty has been taken into account for the mineral reconstruction (Table 3). Magnesium and sodium are measured by Atomic Absorption Spectrometry (AAS) because their measurement with XRF-NITON is either not possible or not reliable. The sulphur measurements were carried out in two steps to separate sulphates and sulphur minerals. The total sulphur was measured by portable XRF calibrated with respect to ICP-MS measurements. The sulphates were measured by AAS. The preparation of the solution for these measurements was designed to ensure that the part of sulphur coming from sulphides was negligible with respect to sulphates. Finally, the quantity of sulphides was inferred by subtracting the measured sulphate from the total sulphur. Aluminium was measured by laboratory XRF (Brücker) because the precision of the portable XRF measures was not satisfactory for this element. The concentrations in Table 2 are expressed with respect to the mass of each class. Because the material is not perfectly distributed over the different grain size fractions, copper may appear more concentrated in some classes.

From these observations, the mineral modal distributions are reconstructed based on the simplified mineralogical content described in Table 3. The available moles of each element were progressively attributed to each mineral phase as described in Appendix A.

2.2 Experimental column leaching

The leaching procedure for the laboratory experiments (Fig. 3) consists in circulating a leaching solution through a column containing one of the grain-size fraction (Table 1). The experiments for the C1 columns are not presented here because the small particles appeared to circulate within the column, which was perturbing the fluid flow and causing clogging and leakage. Only the results for the grain size fractions C2 to C4 are therefore presented. The columns have an internal diameter of 5 cm. They are filled with 250 g of crushed rock placed on a fabric cloth for spreading the entry flow. The crushed rock reaches 15 cm high, which corresponds to a total volume of 294.5 mL. The total pore volume is measured as the injected volume when the top of the rock bed is flooded. It slightly varies with respect to the

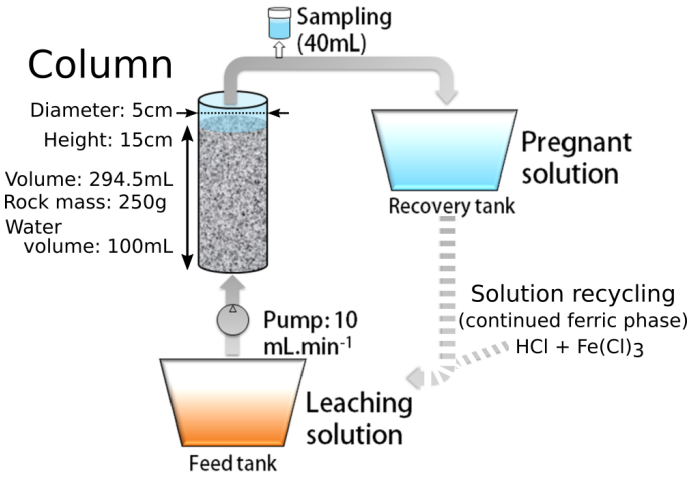

Figure 3 Settings of the column leaching experiments. The leaching solution and duration of each leaching phase are described in Table 4. The recycling of the leaching solution is only used for extending the ferric phase of some experiments after the feed tank has been emptied (c.f., Section 2.2).

Table 4 Description of the three experimental phases.

Phase	Leaching solution	Duration	pH
Water	Pure demineralised water	6 hours	7.01
Acid	HCl 0.1 M	6 hours	0.78
Ferric	HCl 0.1 M + $FeCl_3$ 0.18 M	19 days	0.77

grain size fraction, and ranges from 100 mL to 102 mL, for a total porosity of 34 %.

Three stages are successively implemented according to the parameters summarised in Table 4: (1) water-washing, (2) acid leaching, and (3) ferric-acid leaching. They are designed for progressively dissolving: (1) halogen and sulphate salts, (2) atacamite and carbonate minerals, and finally (3) copper bearing sulphides. In these experiments, the leaching solutions are generated by using chemicals instead of microorganisms as proposed in the final process [Filippov et al., 2017; Matthies et al., 2017; Pakostova et al., 2018]. This limitation is mitigated by the fact that, in the proposed process, the microorganisms would be gathered in a separate bioreactor, whose outlet would be used as an injection solution. Here, we make the assumption that the ferric-acid leaching solution presented in Table 4 correctly emulates the solution that would be produced by the microorganisms in the process conditions. It is supported by the fact that they have similar chemical composition [Pakostova et al., 2018], with the noticeable difference that HCl was used instead of H_2SO_4 for technical reasons, as discussed in Section 5.

During each phase, the column is fed with solution taken from a 20 L tank, which provides enough solution for continuing the experiment for the whole water and acid phases. For the ferric phase however, the solution of the output tank is reused and regenerated by HCl and $FeCl_3$ until the initial pH and redox potential are restored as per the closed circuit illustrated in Fig. 3. This facilitates a significant extension of the ferric-acid leaching phase and enables the evaluation of possible maximum recovery. However, the results of both the water and acid leaching phases, as well as for the first 200 circulated pore volumes of ferric-acid leaching

phase, are obtained from fresh leaching solutions (Fig. 4A-D). The recycling of the leaching solution only affects the latest stages of the ferric-acid leaching (Fig. 4E). During this latest stage, copper progressively accumulates in the output solution and gets re-injected with the recycled solution. The incremental extraction is therefore calculated from the difference between the copper concentrations of the drainage and injected leaching solutions. Another consequence is that the obtained extraction rate should be considered as a minimal estimation because it would be limited by the copper already present in the feeding solution. However, numerical simulations have been carried out with small concentration of copper in the leaching solution, which corresponds to the concentration measured during the recycling stage, and this does not significantly affect the overall copper recovery.

The flow rate and composition of the outlet of the column are regularly measured by sampling 40 mL of solution. The flow rate exhibited an average of 8 mL per minute, but is observed to vary between extremes of 5.5 mL and 11.5 mL per minute. The concentration of chlorine is recorded during the water leaching phase to evaluate the progress of salt mineral dissolution. The concentration of chlorine in solution was measured by spectrophotometry, but it was observed visually that the output solution was slightly coloured, which is interpreted as the effect of the dissolution of iron-bearing sulphates. Therefore, the concentrations of chlorine measured by spectrophotometry were highly overestimated during the water-washing phase. They were corrected by globally rescaling the chlorine concentration of each experiment in order for the cumulated recovered chlorine during the water-washing phase to equate the total measured chlorine in the grains minus the estimated chlorine recovered from atacamite during the acid leaching phase. During the acid leaching phase, copper and calcium are measured by portable XRF calibrated by solutions of known concentration. Finally, during the ferric-acid leaching phase, only copper is measured, with a correction to account for injected copper after the recycling starts.

The experiment has been carried out twice for C3 and C4 to appreciate the repeatability of the obtained results. Repetitions are respectively referred to as C3a and C3b, and C4a and C4b. It was not possible to repeat the C2 experiment for lack of rock material. While the C3a and C4a experiments were limited to the first few hours of ferric-acid phase, the C3b and C4b experiments were run for a longer period to evaluable the possible final copper recovery. The breakthrough curves of the different experiments are reported in Fig. 4. The results are presented in the form of each element mass recovery during a given phase with respect to the number of circulated pore volumes. This is to allow dimensionless comparison between the different series and to lower the effect of previous leaching stages on the next ones. Here, we prefer recovery rather than concentration as it conveniently prevents the output curves from crossing each other. Concentration breakthroughs are presented in Section 3.2.

Uncertainties are carefully examined, which is particularly important for comparing experimental and numerical results. Estimated uncertainties encompass possible errors of concentration measurement, calibration errors, errors and representativity of flow rate measurements, and finally possible integration errors while estimating the extraction

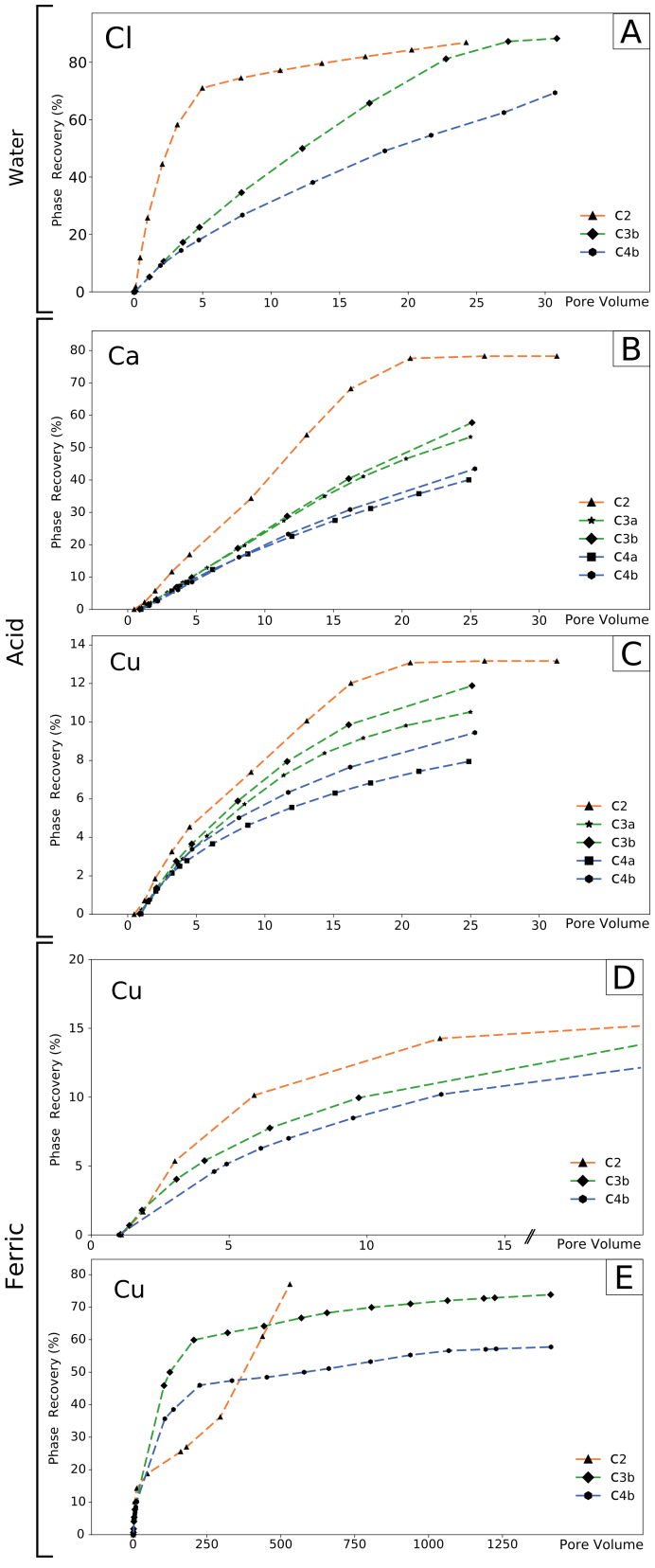

Figure 4 Experimental breakthrough curves for the different grain-size fractions. A: chlorine recovery during the water-washing phase. B: calcium, and C: copper recovery, during the acid leaching phase. D: copper recovery during the beginning of the ferric-acid leaching phase. E: copper recovery during the whole ferric-acid leaching phase (injected copper due to the recycling has been removed).

curve from instantaneous concentrations. For the latest, particular care was taken for the initial points for which the uncertainty about the actual timing of the first breakthrough and intensity of the first concentration peak were considered. Uncertainties are not reported in Fig. 4 to prevent the different curves from overlapping, especially in the initial stages of each phase. However, they are presented in Fig. 6 to 8 where they allow comparison with the numerical results.

2.3 Analysis of experimental results

During the first phase of water-washing, the recovery curve of the finest grain-size fraction (Fig. 4A) shows a first stage of fast extraction up to 5 pore volumes, followed by a slower output rate progressively reaching a plateau. Similar behaviour is observed for column C3b even if the first stage lasts for about 25 pore volumes. For C4b instead, the first fast washing stage is not completed at the end of the water phase. There is a clear effect of the grain size on the extraction, as the extraction rate appears to become slower when the diameter of the grains increases. The water-washing stage seems to be relatively efficient as most of the chlorine tends to be removed from the grains, even if a longer washing period would have been necessary for C4b. The remaining chlorine at the end of this stage corresponds to the chlorine contained in atacamite, which is not efficiently dissolved by neutral pH water.

Similar observations are made for calcium and copper during the acid leaching phase (Fig. 4BC). The curves present an initial fast extraction stage, followed by a slower stage, which appears more clearly for C3 and C4, than for C2. A plateau is finally reached by the C2 curves. Considering the minerals observed within the fresh rock samples (Section 2.1), the calcium recovered during the acid leaching phase would be derived from the dissolution of carbonates, while the recovered copper is assumed to be derived from the atacamite. From the experimental results, both carbonates and atacamite are assumed to be completely dissolved at the end of the acid leaching phase for the C2 column. This hypothesis will be tested numerically in Section 3.3. The effect of grain size on the extraction rate is also observed for copper during the beginning of the ferric phase (Fig. 4D). The results are less clear in the continued ferric leaching phase, when the feeding solution starts being recycled from the output solution (Fig. 4E). The relative position of the C3b and C4b curves remains as expected but C2 extraction rate significantly slows down before increasing again, which causes its curve to cross the others. It is interpreted as problems of fluid circulation within C2 column after the beginning of the injection solution recycling. The results presented in Fig. 4D are not affected by this caveat because they stop before the recycling of leach solution.

The overall copper recovery, including both acid and ferric phases, is still significant for each grain size fraction, as it amounts to 90 % for C2, 86 % for C3, and 67 % for C4, even if the slope of the recovery curves in Fig. 4E suggests that higher recovery could be achieved by further extending the experiment. The observed effect of grain size on the extraction rates clearly supports an increasing limitation of mass transfer with the increase of grain size. This hypothesis is further investigated with numerical models in Sections 3 and 4.1.

In addition, a variation of the total copper extraction would possibly relate to occlusion phenomenons within the internal porosity of the grains. However, this effect is not clearly observed in the results from Fig. 4. The recovery curves suggest that similar recovery values could be reached for all the grain size fractions provided that the experiments are run long enough. Only the results from the extended ferric phase could point toward a variation of total recovery due to occlusion, but this observation is also mitigated by a possible effect of the recycling of the leaching solution. For these reasons, possible occlusion effects are neglected in the proposed numerical models.

3 Numerical modelling of column experiments

In this section, we present a numerical model for simulating the progress of the three leaching stages implemented in the column leaching experiments from Section 2. The numerical models, introduced in Section 3.1, are based on a one-dimensional reactive transport approach where dissolution reactions are driven by the chemical reaction kinetics. Numerical results are compared with experimental results (Section 3.2), which yields a refined understanding of the possible evolution of the outlet composition, as well as the progress of mineral dissolution fronts. Single and dual porosity models are compared as a way to investigate the effect of grain size on the leaching process. The simulated evolution of the mineralogical changes within the columns also makes it possible to observe the propagation of different dissolution fronts throughout the leaching process, which is further discussed in Section 3.3.

3.1 Numerical model of column leaching

The proposed numerical model relies on a one-dimensional discretisation of advective, diffusive, and dispersive transport along the columns, coupled with chemical reactions (Fig. 5). They are implemented in PhreeqC [Parkhurst and Appelo, 1999, 2013].

We propose two versions of this model. The first one considers a single porosity medium, which is used as a reference that ignores mass transfer limitations in the column. The second type of model uses a dual porosity approach [Brusseau et al., 1989; Parkhurst and Appelo, 1999] as a mean for investigating the effect of grain size, which is suggested to better describe mass transport within the system. In the single porosity model, the reactive transport of the flowing leaching solution is based on the following advection-reaction-dispersion (ARD) equation [Parkhurst and Appelo, 1999]:

$$\frac{\delta C}{\delta t} = -\nu_\phi \frac{\delta C}{\delta x} + D_L \frac{\delta^2 C}{\delta x^2} - \frac{\delta q}{\delta t} \quad (1)$$

where C is the concentration in the advecting solution (mol/kg of water), t is time (s), ν_ϕ is pore water flow velocity (m/s), x is the distance along the column (m), D_L is the hydrodynamic dispersion coefficient (m^2/s) combining the effective diffusion coefficient (D) and the mechanical dispersion coefficient (D_m). The parameter q represents the concentrations in the solid phase (mol/kg of water in the pores) so that $\frac{\delta q}{\delta t}$ is the change in concentration in the solid phase due to dissolution and precipitation reactions. The parameters ν_ϕ and D_L are assumed to be equal for all solute species. With this assumption, C may represent the concentration of any element, including all redox species.

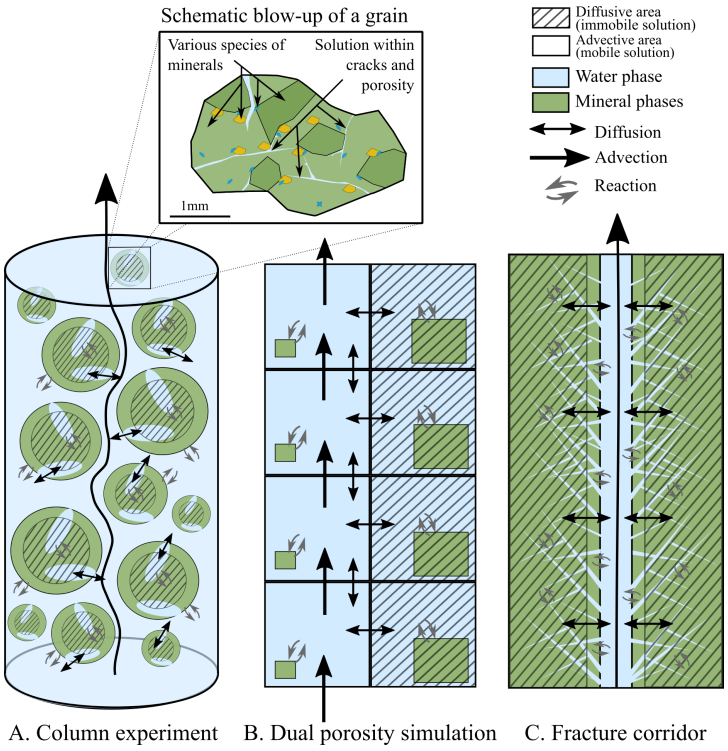

Figure 5 Layout and interactions of the mobile and immobile areas of the proposed numerical model. The column experiments (A) are approached by a dual porosity model (B). The circulation within fracture corridors (C) as modelled in Section 4 are approximated by a similar dual porosity model (B) with adapted dual porosity parameters.

The effective diffusion coefficient is considered negligible in comparison to the mechanical dispersion term.

On the contrary, the dual porosity model considers two zones (Fig. 5): (1) a mobile zone, also referred to as advective zone, where both advection and diffusion occur, but where the advection is the dominant phenomenon, and (2) an immobile zone, also referred to as diffusive zone, where there is no advection and where only diffusion occurs.

The advective zone encompasses the leaching solution that circulates between the grains and a relatively easily accessible portion of the grains, where the leaching solution is able to flow within the grain porosity. The diffusive zone (hatched area in Fig. 5) corresponds to the portion of the grains where the solution contained in the internal porosity is only exchanging by diffusion with the flowing solution of the advective zone. The minerals that are in contact with the flowing solution (between and within the grains) are assigned to the advective zone, whereas the minerals that are only in contact with the immobile solution are assigned to the diffusive zone.

Advection is only allowed between the successive advective cells and each diffusive cell only exchanges with its associated advective cell by a first order approximation of diffusion process [Parkhurst and Appelo, 1999]. This mass exchange is controlled by the first-order exchange coefficient (α). The reactive transport model from Eq. (1) is modified as follows for the dual porosity model:

$$\phi_{aq}^{adv}\frac{\delta C^{adv}}{\delta t}+\phi_{aq}^{dif}\frac{\delta C^{dif}}{\delta t}=-\phi_{aq}^{adv}\nu_{\phi}\frac{\delta C^{adv}}{\delta x}+\phi_{aq}^{adv}D_L\frac{\delta^2 C^{adv}}{\delta x^2}-\phi_{aq}^{adv}\frac{\delta q^{adv}}{\delta t}-\phi_{aq}^{dif}\frac{\delta q^{dif}}{\delta t} \quad (2)$$

$$\phi_{aq}^{dif}\left(1+\frac{\delta q^{dif}}{\delta C^{dif}}\right)\frac{\delta C^{dif}}{\delta t}=\alpha\left(C^{adv}-C^{dif}\right) \quad (3)$$

where ϕ_{aq}^{adv} and ϕ_{aq}^{dif} represent fluid volume fractions in the advective and diffusive zones respectively defined by Eq. (4). The parameters C^{adv}, q^{adv}, C^{dif}, and q^{dif} denote the concentration of any species in the solution and solid phase, of the advective and diffusive zones respectively.

Both models are discretized with an explicit finite difference scheme [Parkhurst and Appelo, 1999]. The system is solved with a split-operator approach, i.e., the chemical reaction term involving q is computed separately between each transport step. The time steps for the transport operator are computed to reproduce the average flow rate observed during each phase for each column. A Courant number of 1 is assumed, i.e., a time step corresponds to the transfer of the whole volume of a cell into the next one at the observed flow rate. It is computed by dividing the total injected solution by the duration of the corresponding leaching phase, which averages at around 8 mL per minute. Because the actual flow rate was observed to slightly vary during the experiment, this approximation partly explains small discrepancies between experimental and numerical observations. Cauchy boundary conditions are used at the extremities of the column as suggested by Parkhurst and Appelo [1999] for laboratory columns with inlet tubing much smaller than the column section. This condition controls the concentration C_0 outside the inlet of column and the flux at both ends.

PhreeqC holds no geometrical description of the reactive medium besides the masses of the respective solution and solid phases. These masses are computed with respect to the level of the dicretisation (number of cells) and the considered model (single or dual porosity). In any case, the total amount of solid and solution is set to reproduce the experimental conditions (c.f. Table 5).

Table 5 Summary of the main modelling numerical parameters.

Temperature (T)	21.5 °C
Grain internal porosity (ϕ)	0.1
Diffusion coefficient (D)	10^{-9} m^2/s
Column volume (V)	295 mL
Rock mass (M_{mx})	250 g
Water volume (V_{aq})	100 mL
Average flow rate (Q)	10 mL/min
Average pore velocity (ν_{ϕ})	2×10^{-4} m/s
Mechanical dispersion (D_m)	10^{-4} m^2/s

For the single porosity model, the grain minerals are equally distributed along a given number of cells, with the circulating solution passing successively from one cell to the next. In the dual porosity models, each cell is thus further divided up into an advective cell and a diffusive cell (Fig. 5B).

The solution and minerals are divided up between the advective and diffusive cells as follow:

$$\begin{aligned}
\phi_{grain} &= \frac{V - V_{aq}}{V\,(1-\phi)} \\
\phi_{aq}^{adv} &= \phi\ \%_{adv}\ \phi_{grain} + \left(1 - \phi_{grain}\right) \\
\phi_{aq}^{dif} &= \phi\ \left(1 - \%_{adv}\right)\ \phi_{grain} \\
\phi_{mx}^{adv} &= (1-\phi)\ \%_{adv}\ \phi_{grain} \\
\phi_{mx}^{dif} &= (1-\phi)\ \left(1 - \%_{adv}\right)\ \phi_{grain}
\end{aligned} \tag{4}$$

where ϕ_{grain} represents the grain volumetric fraction, ϕ_{aq}^{adv} and ϕ_{aq}^{dif} are the volumetric fractions of solution respectively in the advective and diffusive cells, ϕ_{mx}^{adv} and ϕ_{mx}^{dif} are the volumetric fractions of solid phases respectively in the advective and diffusive cells, ϕ is the porosity within the grains, and $\%_{adv}$ is the advective percentage, which corresponds to the volumetric fraction of the grains that is assigned to the advective zone. The internal porosity of the grains (ϕ) is set to 0.1, which corresponds to the measured porosity in the mineralised zones (Section 2.1).

The first-order dual porosity approach implemented in this paper is parameterised by two factors: the advective percentage ($\%_{adv}$) and the exchange coefficient (α). The exchange factor α (s^{-1}) is a first order coefficient to quantify the mass transfer between each advective cell and its associated diffusive cell. According to van Genuchten [1985], Eq. (5) theoretically relates α to the diffusion coefficient D_e inside the diffusive area (m^2/s), the fraction of volume θ_d occupied by the solution in the diffusive zone, and geometrical parameters a (m) and $f_{s\to1}$, under simplifying assumptions:

$$\alpha = \frac{D_e\ \theta_d}{\left(a f_{s\to1}\right)^2} \tag{5}$$

The parameter a represents a characteristic length (m), and $f_{s\to1}$ is a dimensionless shape factor that has different tabulated values depending on the geometry of the diffusive zone (Table 6). While the rock grains from experimental columns are approached as spheres, this model could be adapted to fracture corridors (Fig. 5C) by considering the diffusive areas as infinite half planes.

Table 6 Shape factors for exchange coefficient calculation.

Diffusive region	a (m)	$f_{s\to1}$
Sphere	radius	0.210
Fracture corridor walls	penetration length	0.533

In practice, choosing the right parameters for computing α from Eq. (5) is not trivial. There is no predefined rules for inferring θ_d, and the exchange coefficients obtained with Eq. (5) have been observed to be several order of magnitude too high to reproduce experimental data, even when considering lower diffusion coefficient. Instead of using this equation, applicable values for the exchange coefficient (α) and the advective percentage ($\%_{adv}$) have thus been explored by an exhaustive search. The best observed parameters are reported in Section 3.2. A relationship between α, θ_d, and the grain size is observed and discussed in Section 4.1.

The mineralogical content is based on the reconstruction presented in Table 3. Minerals are allowed to dissolve but precipitation is disabled as a simplification. The dissolution reactions are taken from the Thermoddem* database [Blanc et al., 2012] as described in Table 7. In this paper, the dissolution reactions are treated by a kinetic approach, whose kinetic rate equations are detailed in Appendix B.

Reactive rates are found to be relatively sensitive to temperature, particularly for the carbonate dissolution under the experimental conditions. Unfortunately, the laboratory temperature varied by a few degrees during the experiments. An average temperature of 21.5 °C is used for the numerical simulations, as it would be difficult to accurately record and account for these daily variations.

Three successive stages are implemented as in the laboratory experiments. The injected solution is computed to match exactly that used in the experiments (Table 4). The simulations presented here stop at the end of the first part of the ferric-acid leaching stage, before the recycling of the leach solution starts. As a result, the simulated leach solutions are not affected by possible re-injected elements.

PhreeqC imposes an initial equilibration of the solutions of the column cells before the first reactive transport stage. To avoid convergence issues, the solutions are equilibrated beforehand with a solid phase that bears the mineralogical content shown in Table 3, but the dissolved minerals are restored to their initial content before the reactive transport starts.

The dissolution front observed during the simulated acid leaching phase is very sharp (see the sharp front of atacamite dissolution in Fig. 9). It is causing oscillations of the calcium and copper breakthrough curves when using too few cells. Fortunately, these curves are converging toward a stable solution when the number of cells increases. The dissolution fronts occurring during the ferric leaching phase are smoother and enable appropriate results even with a limited number of cells. We have thus been able to use a relatively coarse discretisation (60 to 80 cells in total for the dual porosity scheme) for exploratory tests and for the ferric phase, while 800 cells (advective and diffusive cells altogether) were necessary for refined results during the acid leaching phase. An artificially high longitudinal dispersivity of 2 m has also been used to further attenuate these oscillations. It yields a mechanical dispersion of $10^{-4}\ m^2 s^{-1}$ considering a relatively small pore velocity of $2 \times 10^{-4}\ m\,s^{-1}$ estimated within the columns, which is integrated within the term D_L in Eq. (1). Sensitivity tests have shown that this dispersivity is sufficient to attenuate the artefacts without significantly affecting the breakthrough and recovery curves at the scale of the observed durations.

3.2 Analysis of the simulated copper breakthrough

The output obtained from the models that are the closest to experimental results are presented in Fig. 6-8. The dual porosity parameters are: C2 ($\%_{adv}$:80%, α:$10^{-3.6}s^{-1}$), C3 ($\%_{adv}$:75%, α:$10^{-3.9}s^{-1}$), C4 ($\%_{adv}$:65%, α:$10^{-4.05}s^{-1}$). The results of the single porosity models are also presented for a comparison. The experimental and numerical results are compared based on the observed and simulated outlet concentration, and recovery of both copper and calcium. Chlorine was also considered but it appeared difficult to compare during the water-washing stage because of the initial amount of chlorine present in the numerical model. During the other phases, the injected chlorine is also preventing

*http://thermoddem.brgm.fr/

Table 7 Dissolution reactions for the minerals involved in the reactive process with the corresponding equilibrium constants at 25 °C. The equations and equilibrium constants are taken from the Thermoddem* database [Blanc et al., 2012], except for the ankerite, which is adapted from Krupka et al. [2010].

Mineral	Reaction	$\log_{10}(K)$
Halite	$NaCl = Na^+ + Cl^-$	1.594
Thenardite	$Na_2SO_4 = 2\,Na^+ + SO_4^{2-}$	-0.340
Calcite	$CaCO_3 + H^+ = Ca^{2+} + HCO_3^-$	1.847
Dolomite	$CaMg(CO_3)_2 + 2\,H^+ = Ca^{2+} + Mg^{2+} + 2\,HCO_3^-$	3.533
Ankerite	$CaFe(CO_3)_2 + 2\,H^+ = Ca^{2+} + Fe^{2+} + 2\,HCO_3^-$	-0.311 [Krupka et al., 2010]
Atacamite	$Cu_4Cl_2(OH)_6 + 6\,H^+ = 2\,Cl^- + 4\,Cu^{2+} + 6\,H_2O$	14.918
Anilite	$Cu_{1.75}S + H^+ = 1.5\,Cu^+ + 0.25\,Cu^{2+} + HS^-$	-31.220
Bornite	$Cu_5FeS_4 + 4\,H^+ = 4\,Cu^+ + Cu^{2+} + Fe^{2+} + 4\,HS^-$	-107.495
Pyrite	$FeS_2 + 0.75\,H_2O = Fe^{2+} + 0.25\,S_2O_3^{2-} + 1.5\,HS^-$	-23.590
Microcline	$KAlSi_3O_8 + 4\,H^+ + 4\,H_2O = Al^{3+} + K^+ + 3\,H_4SiO_4$	0.004
Kaolinite	$Al_2Si_2O_5(OH)_4 + 6\,H^+ = 2\,Al^{3+} + 2\,H_4SiO_4 + H_2O$	6.471
Quartz	$SiO_2 + 2\,H_2O = H_4SiO_4$	-3.737

any reliable comparison between simulated and observed chlorine breakthrough.

The results of the simulation of C2 column (i.e., the smallest grain size), are relatively well matching the experimental copper breakthrough during the acid phase (Fig. 6). There are some discrepancies between the numerical and the experimental results. Namely, the simulated curve falls outside the uncertainty range of some points. This can be attributed to several factors including the fact that the size of the particles of the experiments might not be perfectly distributed causing variations of the breakthrough mainly in the early stages. Variations of flow and temperature could also be responsible for small variations of copper production. These uncertainties were more difficult to estimate and have not been included in the presented error bars, but they could explain why the numerical results are not always matching the data. Besides these caveats, we observe that the single porosity model already fits the data quite well. Actually, the main deviation from the experimental data applies to the last part of the breakthrough curve, which is a little too high shortly after 15 pore volumes. It also stops too soon and fails to reproduce the observation of a remaining concentration of copper at around 20 pore volumes. By comparison, the dual porosity model is capable of matching the last data points and maintains a copper breakthrough up to the observed data point. The proposed dual porosity model is therefore considered as slightly better than the single porosity model for reproducing the observed data. Overall, the best-fit dual porosity model is observed to converge towards a breakthrough that is very close to the breakthrough of the single porosity model. This supports the hypothesis that the mass transfer limitations are almost negligible, as expected for the smallest grain sizes. The results for the ferric leaching phase are less conclusive. Both recovery curves are matching the data quite well, but they are underestimating the first peak of copper breakthrough. This is related to the observation from Fig. 9 showing that the ferric phase is more sensitive to kinetics than to the selection of either single or dual porosity. These observations may signify that the kinetic rates and/or the relative proportion of bornite and anilite could have to be revised.

Similar observations are made from the results of C3 grain size simulations (Fig. 7). The discrepancies between single and dual porosity models are more visible, namely because the single porosity model does not reproduce the data as well as for C2 experiments. The copper breakthrough is, once again, too high towards the end of the breakthrough curve and coming to an end too soon. The dual porosity model overcomes these weaknesses by predicting the concentration to drop slightly at around 17 pore volumes and to remain at the level observed for the data points up to the end of the phase. The first peak of the ferric phase output is better predicted than in C2 experiments but the following output is also slightly overestimated. However, this effect is mitigated by the dual porosity model, which appears to more closely emulate the observed data points than the single porosity model.

Finally, similar observations are also made for the C4 experiments. Here, the single porosity model seems even more inadequate as the breakthrough is clearly stopping too soon during the acid phase, which is causing the recovery curve to fall completely outside the uncertainty range of the last data points. It is also clearly overestimating the breakthrough during the ferric phase. On the contrary, the dual porosity model follows the concentration and recovery curves. The only observed limitation is for the breakthrough curve between 10 and 15 pore volumes. The copper breakthrough suddenly drops before going up again at the level observed in the experimental data. This is in fact due to a small gap between the breakthroughs related to the advective and the diffusive parts of the column. It is to be considered as an artefact of discretisation, because the continuous exchange between the outer rim and the core of the grains is approximated by only two zones mixed with a first order exchange coefficient. An improved description of mass transfer kinetics, for example through a finite difference diffusional model [Parkhurst and Appelo, 1999; Van Staden and Petersen, 2018] or a multi-rate model that considers a higher number of exchanging zones [Haggerty and Gorelick, 1995], should improve these results.

Despite some discrepancies, these numerical results show that the experimentally observed breakthrough can be reproduced by a one-dimensional dual-porosity model, even though the kinetics of sulphide dissolution should still be further investigated. The most interesting points illustrated by these results is that the dual porosity approach appears

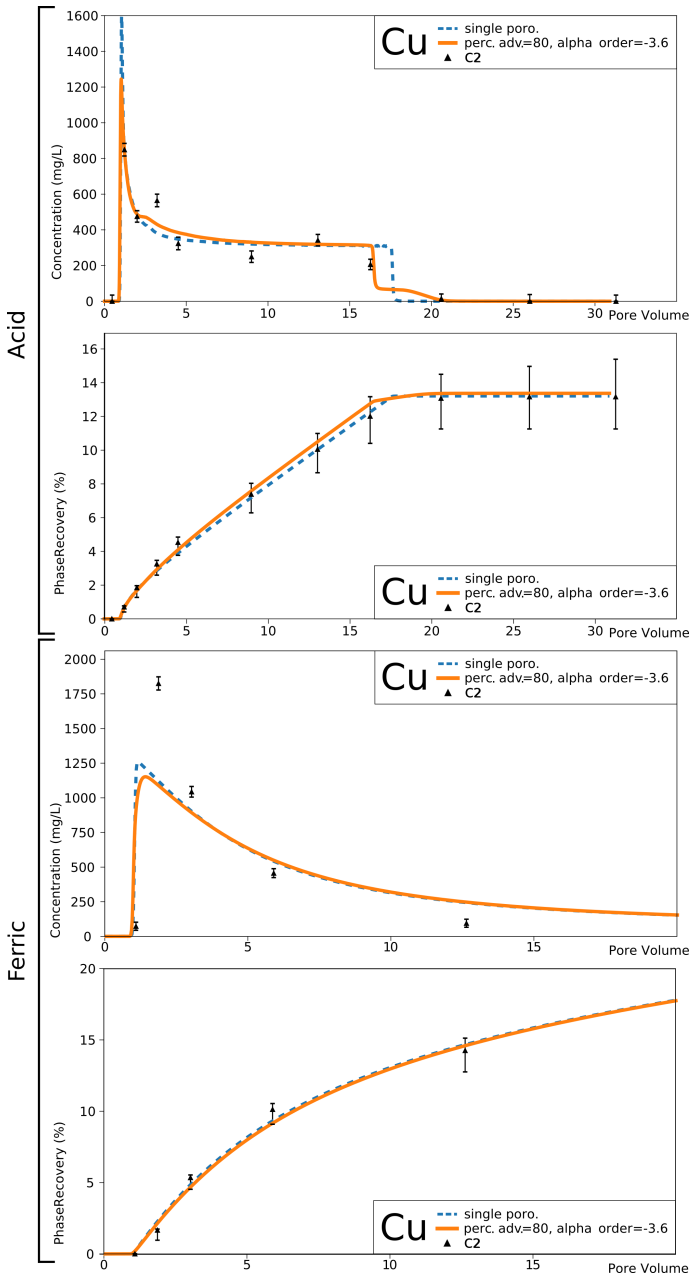

Figure 6 Copper breakthrough and recovery curves for single and dual porosity models of the C2 column. The single porosity model (dotted line) and dual porosity mode (plain line; $\%_{adv}$:80%, α:$10^{-3.6}$s^{-1}) are compared to experimental data (triangles) with associated error bars. Only the first part of the ferric-acid leaching stage is used, which means that the results are not affected by the recycling of the leach solution.

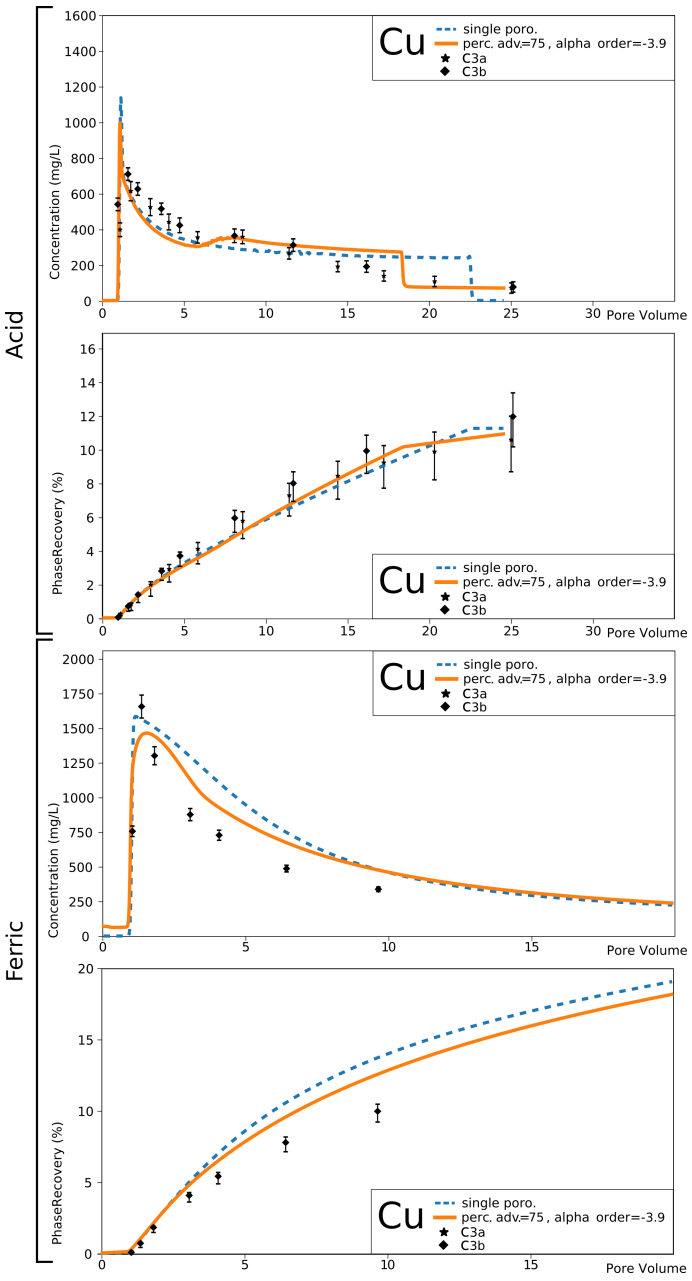

Figure 7 Copper breakthrough and recovery curves for single and dual porosity models of the C3 columns. The single porosity model (dotted line) and dual porosity mode (plain line; $\%_{adv}$:75%, α:$10^{-3.9}$s^{-1}) are compared to experimental data (C3a: stars; C3b: diamonds) with associated error bars. Only the first part of the ferric-acid leaching stage is used, which means that the results are not affected by the recycling of the leach solution.

to be of increasing importance when the grain size grows. This confirms an increase of internal mass transfer limitations with the grain size and hence a slower Cu extraction.

3.3 Simulated mineralogical evolution

Numerical simulations give access to the mineral evolution of the column interior throughout the three leaching stages. The dual porosity simulation of the C2 column (Fig. 9) suggests that halite and thenardite are dissolved in a rapidly progressing front during the water-washing period. The dissolution front is advancing slightly faster in the advective part than in the diffusive part because of the retardation imposed by the first order exchange coefficient α. By the end of this phase, all the halite and thenardite are calculated to have been dissolved from both dual porosity areas, which is in accordance with observed Cl breakthrough (Fig. 6A).

During the acid leaching phase, successive dissolution fronts of calcite, atacamite, and finally ankerite and dolomite, are progressing through the column. The retardation of these dissolution fronts in the diffusive part appears to be more pronounced than during the water-washing phase. Carbonates are simulated to be completely dissolved from the advective part by the end of the acid leaching phase, while a small amount of ankerite and dolomite remains visible toward the end of the diffusive zone. Numerical simulations indicate that atacamite would be efficiently dissolved during the acid leaching phase, which is in agreement with the observed copper extraction during laboratory experiments (Fig. 6C).

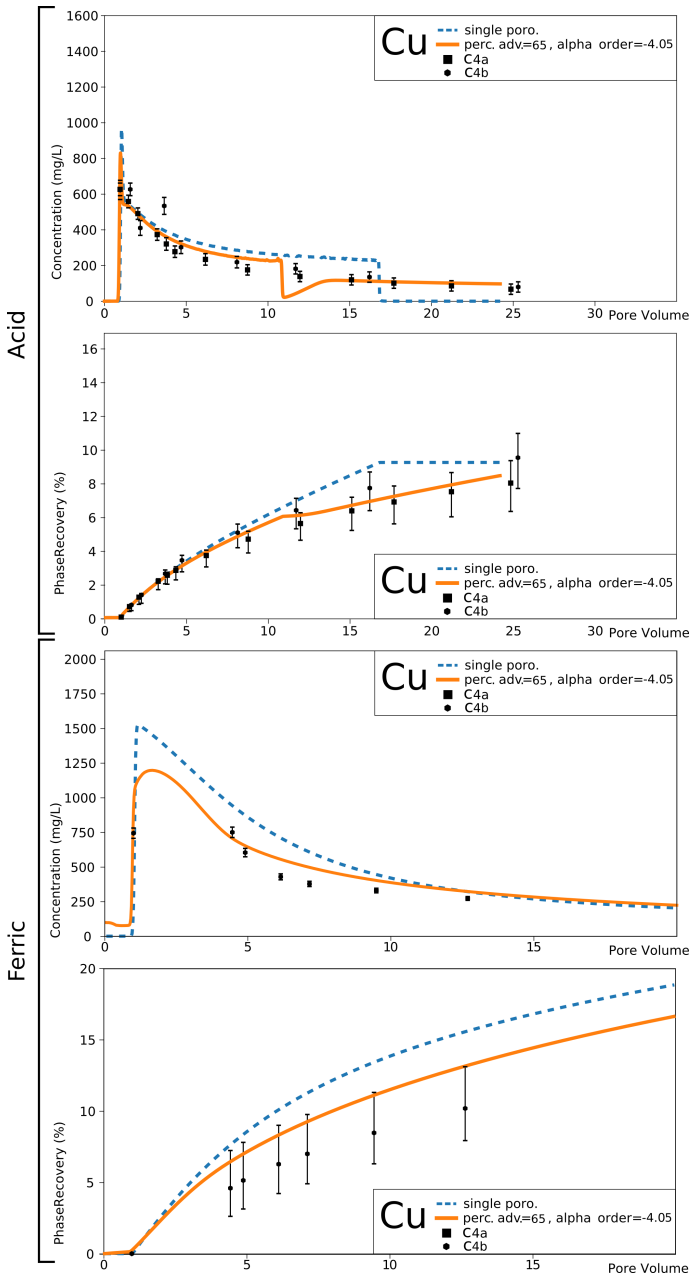

Figure 8 Copper breakthrough and recovery curves for single and dual porosity models of the C4 columns. The single porosity model (dotted line) and dual porosity mode (plain line; $\%_{adv}$:65%, α:$10^{-4.05}$s^{-1}) are compared to experimental data (C4a: squares; C4b: hexagons) with associated error bars. Only the first part of the ferric-acid leaching stage is used, which means that the results are not affected by the recycling of the leach solution.

The different sulphides are only simulated to be efficiently dissolved during the ferric-acid phase. Bornite dissolves first, followed by pyrite, and finally anilite, even though a small proportion remains in the column at the end of the ferric leaching phase. The dissolution of the sulphides is not following as sharp a front as that of the other minerals, but is instead relatively spread out over the entire column. This suggests that this third stage is more sensitive to the relative dissolution rates than to the dual porosity parameters.

As the grain size increases when considering the C3 and C4 grain size fractions, the numerical simulations show an increasing impact of the dual porosity parameters. For larger grains, the retardation is observed to affect even the ferric stage, mainly because of the difference of carbonate leaching efficiency between advective and diffusive parts.

4 Simulations of in-situ conditions

Experimental and numerical modelling, as presented in Sections 2 and 3, provide crucial insights into the physical and chemical processes at play during the leaching of carbonate bearing copper ore. However, the experimental conditions are expected to be quite different from the conditions expected in the proposed in-situ recovery process. For example, temperature would affect the chemical reactions and can be accounted for in the numerical models. In this section, we propose a strategy for dealing with other conditions, such as the effect of grain size, which are more complex to handle.

The results obtained in Sections 2 and 3 clearly demonstrate an effect of the characteristic size of the solid medium on the way copper is recovered. While this relationship is observed on rock samples crushed and sieved at different grain sizes, it seems crucial to consider these aspects for in-situ material. Whether it corresponds to fresh rocks, when natural hydraulic conductivity is sufficient for the process, or to fractured or blasted rocks, if stimulation is required, the effect of the diffusion through the material should be taken into account for applying the proposed model in-situ.

In this section, we propose to further investigate the relationship between the dual porosity parameters and the characteristic dimension of the diffusive medium. A mathematical relationship is proposed to relate these parameters to the grain size in the presented experiments (Section 4.1). Our dual porosity model is further adapted to the case of a fracture corridor (Fig. 5C) as an example of adaptation to in-situ hydrodynamic conditions (Section 4), which first requires the estimation of the length of penetration of the leaching effect (Section 4.2).

4.1 Analysis of the effect of grain size

There appeared to be no reliable theoretical way to infer a priori the appropriate dual porosity parameters for accurately modelling the experiments presented in Section 2. More precisely, there was no trivial way to infer the percentage of grains to be put in the advective part, and numerical simulations showed that Eq. (5) yields exchange factors that are by several orders too high for reproducing the experimental observations.

To overcome these hurdles, an exhaustive search has been carried out for determining the range of acceptable dual porosity parameters ($\%_{adv}$ and α) for each grain-size fraction with respect to the experimental results (Fig. 10).

Ideally, an objective numerical evaluation of each model quality would have been preferred, but this was rendered difficult by a number of factors. For example, as stated earlier in Section 3.1, the sharp dissolution fronts occurring during the acid leaching phase were causing small numerical oscillation of the breakthrough curves. While these oscillations have been shown to disappear and converge toward high-resolution results when the number of cells increases, it was difficult to systematically account for this artefact because of the prohibitive computation cost it would have represented.

The quality of each model as thus been evaluated qualitatively by combining criteria such as the distance between experimental and calculated data points, the volume of circulated solution when the copper breakthrough stopped, and the intensity of the first peak. The results were mainly evaluated based on the copper concentration and recovery

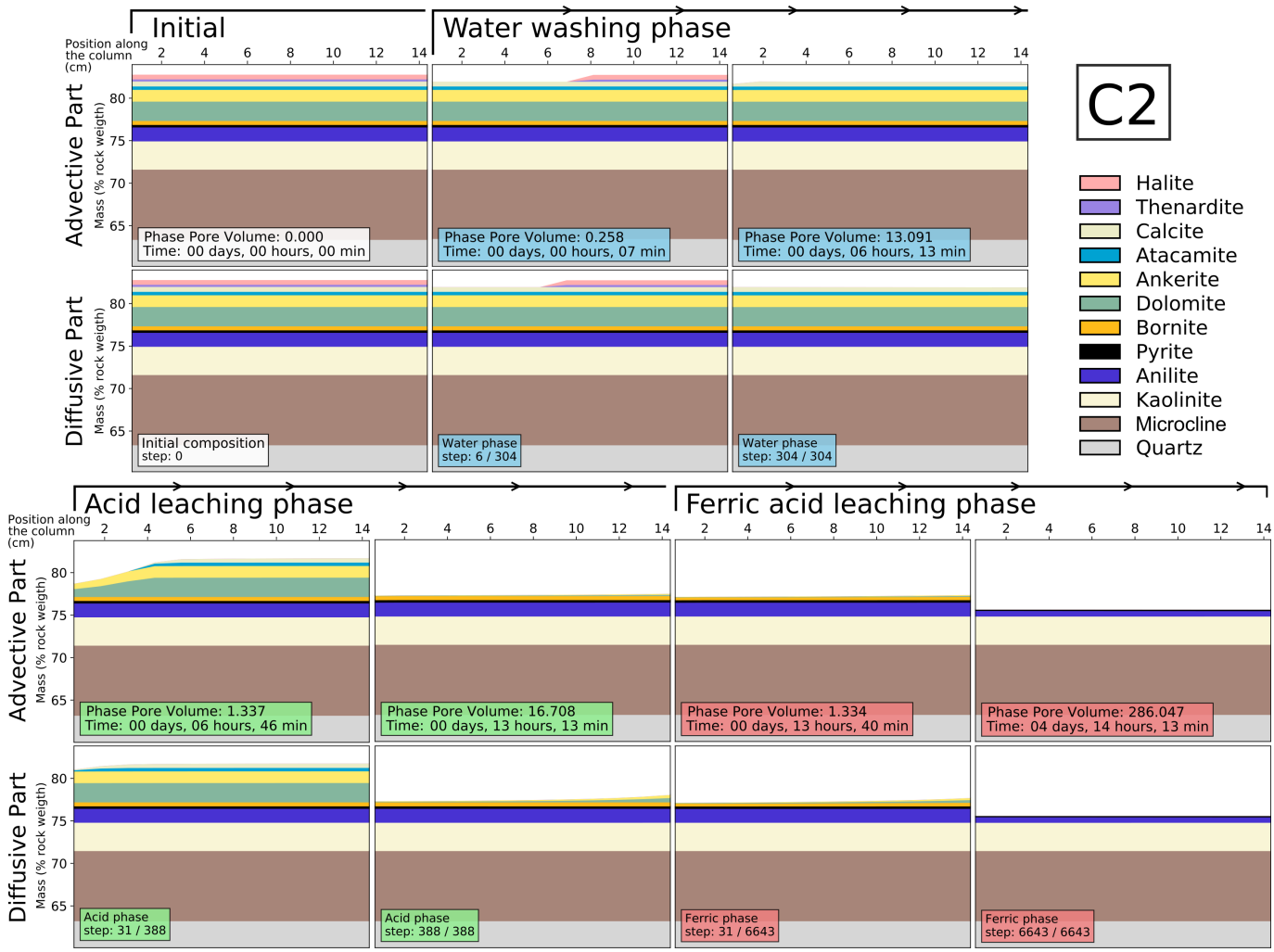

Figure 9 Mineral evolution within the C2 column simulated with a dual porosity model ($\%_{adv}$: 80%, α: $10^{-3.6}\mathrm{s}^{-1}$). The repartition of the different mineral phases along the column are represented as a stacked diagram. The y-axis starts at 60 % because quartz is largely predominant in the mineral composition. The first line represents the advective part, while the second line represents the diffusive part of the column. The first column of the figure illustrates the initial mineral repartition, while the next columns show the evolution through the early and final stages of each leaching phase.

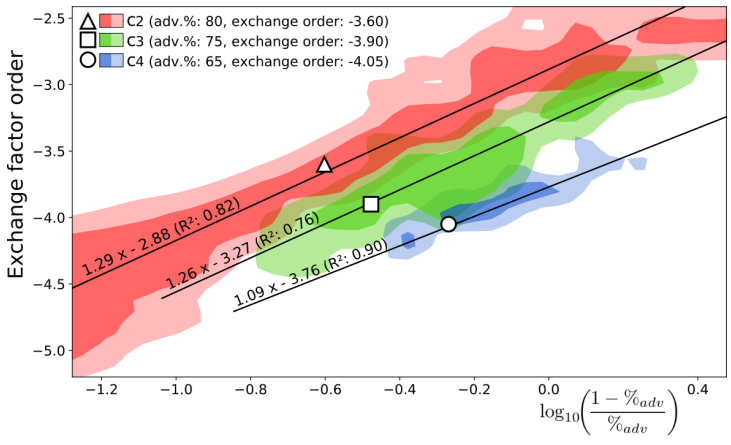

Figure 10 Areas of acceptable dual porosity parameters for each grain size fraction. The level of opacity is in accordance with the qualitative level of acceptability. A linear relationship is observed between the logarithm of the exchange factor and the logarithm of the ratio between the diffusive and advective volumes. The equation of the linear regression (black line) and the coefficient of determination are reported on the graph. The best matching models for C2 (triangle), C3 (square), and C4 (circle), are also presented here. They correspond to the detailed results presented in Section 2.3.

during the acid leaching phase, as it has been observed to be the most sensitive to dual porosity parameters, but the results of calcium breakthrough and copper breakthrough during the ferric leaching phase have also been used as indicators to further refine the model.

From this exploration of dual porosity parameters, it appears that a number of models are able to reproduce similar results as obtained by laboratory experiments. For the C2 experiments, an acceptable exchange coefficient can be found for almost any assumed advective percentage. The range of acceptable parameters is progressively reducing when considering the coarser series, but a trend of acceptable parameters can always be observed. When the logarithm of the exchange factor is plotted with respect to the logarithm of the ratio of diffusive and advective volume, a linear relationship appears (Fig. 10). While the slopes for all the grain size fractions are very similar, the intercept of the regression is decreasing when the grain size grows (refer to Fig. 10 for the linear equations and coefficient of determination). According to the obtained intercepts, a linear relationship can be proposed for relating the intercept to the logarithm of the grain radius (r, in meter), with a coefficient of determination (R^2) of 0.90. This relationship should be further refined by investigating a larger number of grain size fractions, but

the observed relationship already yields a first estimate of acceptable exchange factor with respect to percentage of advective zone ($\%_{adv}$):

$$\log_{10}(\alpha) = p_\varepsilon \log_{10}(\varepsilon) - p_r \log_{10}(r) - b$$
$$\text{where} \quad \varepsilon = \frac{1 - \%_{adv}}{\%_{adv}} \tag{6}$$

The coefficients of Eq. (6) are estimated by linear regression of α with respect to the advective percentage ($\%_{adv}$) and average grain size radii (r) taken from Table 1, which yields: $p_\varepsilon = 1.29 \pm 0.08$, $p_r = 0.956 \pm 0.101$, and $b = 6.17 \pm 0.30$. This equation can be rewritten as a fractal law, where α_0 is the exchange coefficient for a reference case of an intermediate advective zone size (i.e., $\%_{adv} = 0.5$ and $\varepsilon = 1$) with the average radius of C2 (i.e., $r_0 = 4 \times 10^{-4}$ m), which is the most reliable series in our simulation:

$$\alpha = \alpha_0 \left(\frac{\varepsilon}{\varepsilon_0}\right)^{p_\varepsilon} \left(\frac{r_0}{r}\right)^{p_r} \tag{7}$$
$$\text{with} \quad \log_{10}(\alpha_0) = p_\varepsilon \log_{10}(\varepsilon_0) - p_r \log_{10}(r_0) - b$$
$$\text{i.e.} \quad \alpha_0 = 1.20 \times 10^{-3}$$

Equation (7) can be extrapolated and used for estimating possible exchange coefficients for other grain size fractions. For example, Fig. 5 shows the exchange coefficient that should be used for simulating the C1 fraction, for which the laboratory experiments failed because the size of the particles was too small. This equation is also used for extrapolating the exchange coefficient for in-situ conditions as described in Section 4.3.

4.2 Inferring wall penetration length

The distance up to which the different leach solutions affect the host rock would be highly overestimated by considering pure diffusion. In fact, the acidic and redox potentials of the leach solution are rapidly buffered by the reaction with the different minerals within the fracture walls (e.g., carbonates and sulphates). The actual penetration distance is thus expected to be significantly lower than what could be estimated by diffusion only. However, incorporating the reaction in an analytical evaluation of the penetration length is not direct in the analytical formula.

We propose to evaluate the potential penetration length of the reactive fronts by running a numerical model of reactive diffusion through the fracture walls. This model uses the same settings as the single porosity model developed in Section 3 except for the hydrodynamic settings. Here, the entry cell of the one-dimensional model is located within the fracture core, where the leach solution circulates. All the other cells are located within the fracture wall and aligned orthogonally to the fracture plan (Fig. 11). For this model, the transport capabilities of PhreeqC are used in a pure diffusion mode [Parkhurst and Appelo, 1999, 2013], i.e., all the cells are only exchanging by diffusion. A Dirichlet boundary condition sets the composition of the first cell (within the fracture), which follows the same stages as in Section 3. A Neumann boundary condition is set for the last cell of the column and imposes that the diffusion flux is null outside the last cell.

For example, to evaluate the penetration length after 4.5 days, a first model made of 30 cells that covered 10 cm within the fracture wall was run. It suggested that the solution actively penetrates up to only 3 cm after 4.5 days

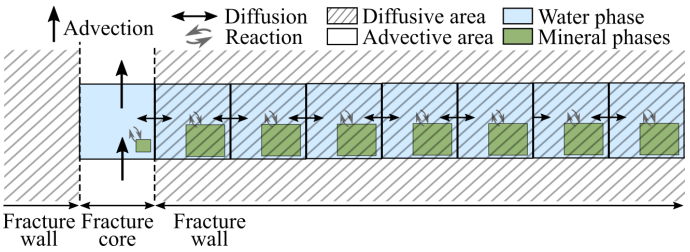

Figure 11 Numerical experiment to simulate the lateral propagation of a leaching front along a fracture corridor.

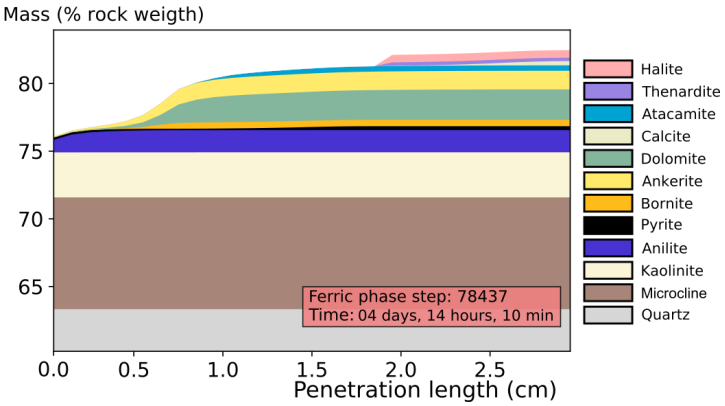

Figure 12 Progress of reactive fronts in the wall of a fracture corridor after 4.5 days of leaching.

based on the resulting mineral repartition within the column. A second model with 30 cells going only 3 cm within the fracture wall was used to refine the simulation.

The discrimination of advective and diffusive parts is not trivial and would evolve through time as the solution further penetrates into the fracture walls. As a first approximation, we propose to consider the area where atacamite has been dissolved at the end of the simulation period as communicating more intensely with the solution that is flowing through the fracture. This criterion yields an advective zone penetrating 1 cm into the fracture wall after 4.5 days (Fig. 12), which would result in an advective percentage ($\%_{adv}$) of 33 %.

4.3 Simulation of leaching along a fracture corridor

In the proposed fracture corridor model, the leach solutions circulate within the core of a fracture and quickly exchange with the volume of rock directly in contact with the fracture walls, while a larger surrounding volume is affected through diffusion only (Fig. 5C). The method proposed in Section 4.2 was applied to evaluate the penetration of the reactive front. From Eq. (7), the exchange coefficient was estimated at $10^{-4.9}$ s^{-1} for an advective percentage of 33 %.

The leaching of such a fracture corridor is simulated by the dual porosity model presented in Section 3.1 and a global mineralogical content corresponding to the global composition of the rock samples, derived from table 3. The fracture core is 1 m long, 1 m high, and has an aperture of 2 mm. Three successive phases are applied as described in Table 4. The duration and flow rates are rescaled to account for the size of the fracture. Water is injected for 46 hours at a rate of 125 mL/min, acid leach solution is injected for 90 hours at a flow rate of 63 mL/min, and ferric-acid solution is circulated for 74 days at a flow rate of 93 mL/min. The model is discretised with 160 cells for simulating the water

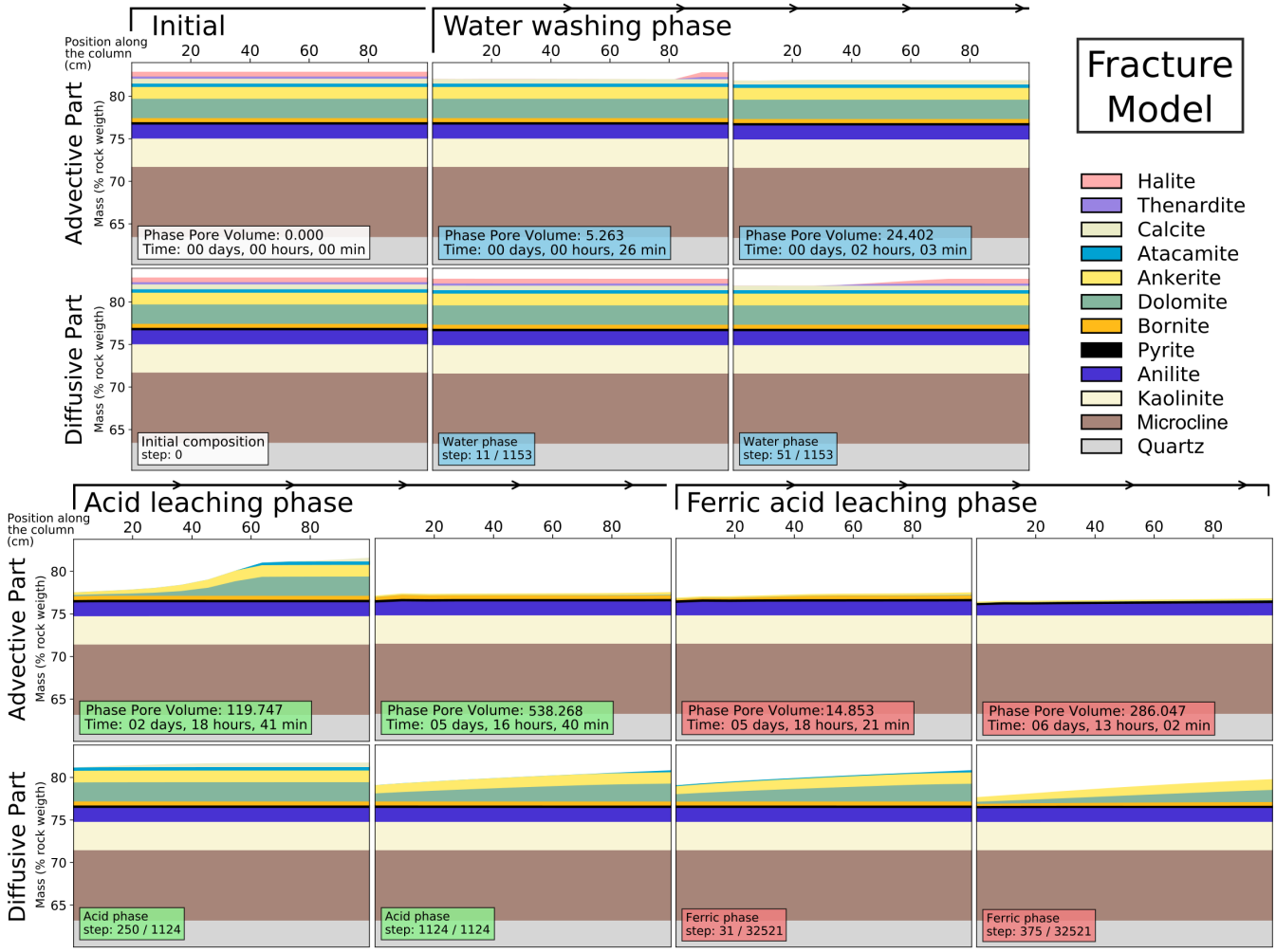

Figure 13 Mineral evolution within the walls of a 1 m long fracture simulated with a dual porosity model ($\%_{adv}$: 33%, α: $10^{-4.9}\mathrm{s}^{-1}$). The repartition of the different mineral phases along the column are represented as a stacked diagram. The y-axis starts at 60 % because quartz is largely predominant in the mineral composition. The first line represents the advective part, while the second line represents the diffusive part of the column. The first column of the figure illustrates the initial mineral repartition, while the next columns show the evolution through the early and final stages of each leaching phase.

and acid leaching phases, and 24 cells for the ferric-acid phase.

The mineralogical evolution of the fracture (Fig. 13) is very similar to the one observed in the numerical simulation of experimental columns (Fig. 9) even if the minerals are dissolved at a slower rate in the diffusive part of the fracture walls as compared to the column experiment. This is in agreement with the lower magnitude of the exchange coefficient estimated for the fracture numerical experiments. A significant amount of carbonate remains in the diffusive part at the end of the acid leaching phase, which suggests that an extended acid leaching phase could have been applied for increasing its efficiency. Similar observations can be made from the breakthrough curve (Fig. 14A), which shows that Ca and Cu remain to be dissolved during that phase.

Remaining carbonates and atacamite are progressively dissolved during the ferric-acid leaching phase, as well as the different sulphides (Fig. 13). Figure 14 shows that the copper extraction becomes very slow after 400 pore volume of ferric-acid solution. After 120 days of the three successive phases, the copper recovery reaches 87 %, and the calcium recovery reaches 67 % (Fig. 14C). The simulated zone of 1 m^2 of fracture with 3 cm of penetration of the leach solution on both sides amounts to about 1 kg of copper extraction. It is associated with an estimated production of 1.12 kg of CO_2 due to the dissolution of carbonates (Fig. 14D). This estimate is to be considered as an upper bound for the possible production of carbon dioxide gas as it accounts for the entire carbon breakthrough, while a significant part would probably remain in solution. This copper recovery and CO_2 production estimates only apply to the volume actually reached by the penetration of the solution within the fracture walls. Global recovery would depend on the density of fractures and might be significantly lower.

5 Discussion

The uncertainties attached to experimental data were carefully examined and are reported in Fig. 6 to 8 (Section 2.2). However, the uncertainties about the flow rate measurements and integration are not accounted for because it appears difficult to provide a reliable estimation. In practice, the average around which the measured flow rate fluctuated has been used to approximate the true rate of flow as a model input.

All the available information has been used during the mineralogical reconstruction, including feedback information from the experimental and numerical simulations (Ap-

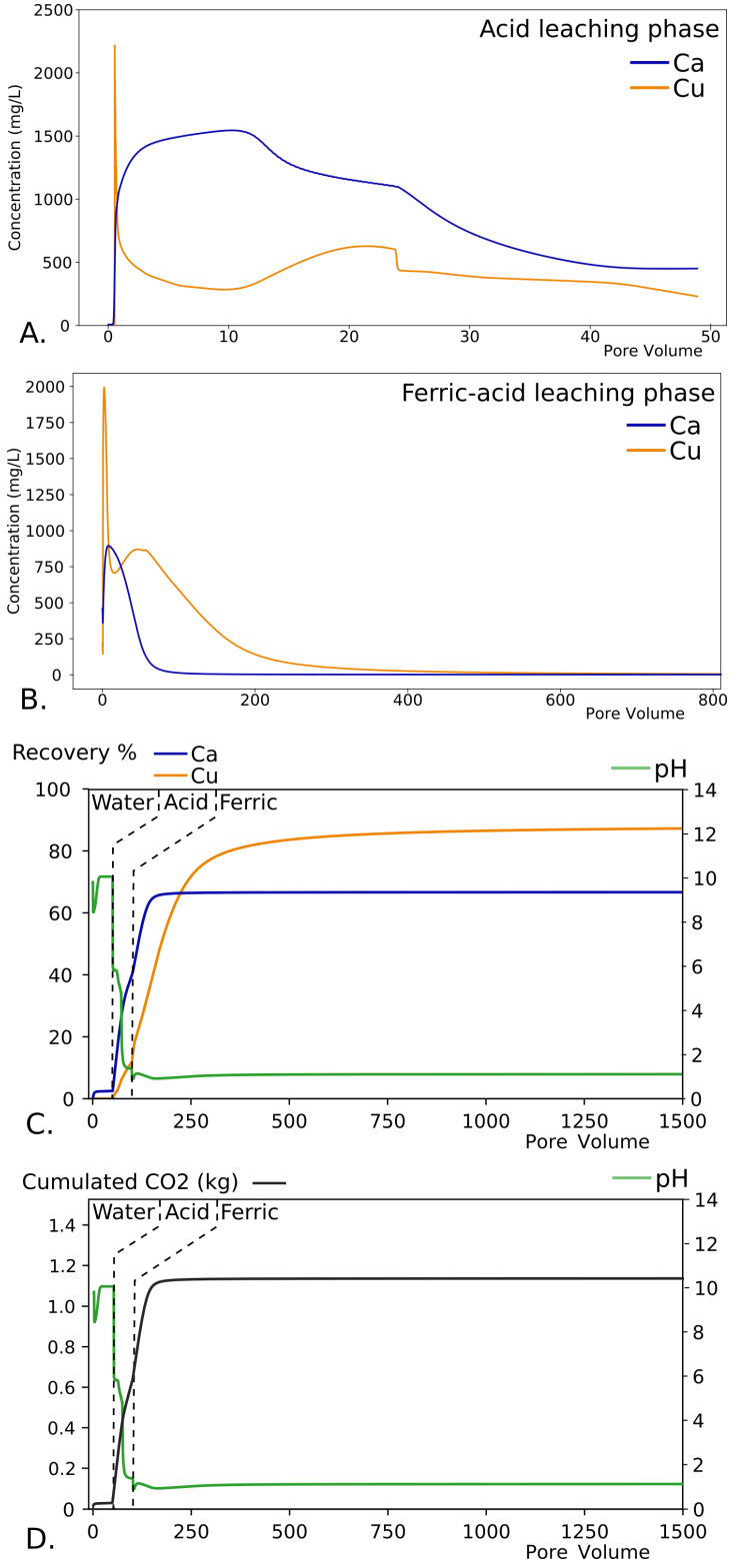

Figure 14 Breakthrough curves for the simulation of the process applied to a fracture corridor. A: acid leaching phase, B: Ferric-acid leaching phase. C: Recovery curves for Ca and Cu, and pH evolution of the outlet, through the three successive phases. D: Cumulated CO_2 production and pH evolution of the outlet, through the three successive phases.

pendix A). For example, the part of copper to be attributed to atacamite was inferred from the plateau observed in the copper extraction during the acid leaching phase of C2 experiments. As the plateau is not reached for C3 and C4, this value was inferred by a manual inversion approach. An initial value was estimated by extrapolating the experimental extraction curves along the observed trend. It was then progressively refined by adjusting this parameter until the simulated curve fitted the experimental data. Uncertainties remain in the mineralogical reconstruction, in particular, the relative proportions of the different carbonates and sulphates might have to be further refined. While the first results presented here are still valid, the long-term simulations, as well as, the start of the ferric stage might remain relatively sensitive to such mineralogical uncertainties.

The kinetic rates of some minerals, in particular the carbonates and sulphides, which also dramatically impact on the numerical results, are subject to uncertainties. We observed that the kinetic rates of carbonates have to be reduced for accurately reproducing the larger grain size fractions (Table 9). This is interpreted as a relative decrease of the available reactive surface in the larger grains, where the minerals have been less efficiently separated from each other during the grinding and sieving process. The surface of carbonate minerals would be better exposed in the smaller grain size fractions than in the larger ones. In any case, the dependence of mineral kinetics to the grain size and to the relative mineral proportions should be investigated to further refine the presented numerical model. Even if this effect was only investigated for the carbonates, it might also apply to the other minerals, including the sulphides, which should be further tested.

During the ferric-acid leaching phase, the numerical models tend to indicate that the dual porosity parameters have a lesser impact on the breakthrough curves as compared to the acid leaching phase. This suggests that the kinetic rate of sulphur dissolution has a higher impact on the copper extraction than the diffusion within the grains, even if the impact of grain size remains significant. Diffusion within the grains still appears to be of first order importance for the larger grain size presented in these experiments (C3 and C4). The inferred exchange rate for the fracture corridor model predicts an even greater effect for in-situ applications, because the penetration of the leach solution through fracture walls is estimated to be larger than the grain size used for the experimental models. This effect is important during the water-washing and causes retardation of the chlorine extraction. The grain size effect is more sensible during the acid leaching phase and greatly impacts the atacamite recovery and removal of carbonates. Diffusion within the grains also appears to cause a retardation of carbonate removal, which has a negative impact on the preparation of the rock for the ferric-acid leaching phase and greatly impacts the copper extraction of this last stage.

Besides the different sources of uncertainty, some conclusions can still be drawn regarding the relationship between the geometry and the transfer coefficient of the dual porosity medium. Equation (6) and Eq. (7) are established from experimental and numerical results based on a medium that consists of sub-spherical grains of various sizes between 0.2 and 8 mm. The proposed model for in-situ condition considers fracture corridors, which have a different geometry and characteristic size. Future experimental studies should thus investigate the applicability of these equations to fracture corridors. Other methods for enhancing hydraulic conductivity such as blasting could also be applied and result in different in-situ geometry for the dual porosity medium. Further experimental studies would be needed for validating the proposed model for fractured or blasted in-situ medium. While the proposed model from Eq. (7) makes no explicit

assumption about the medium geometry, it would be interesting to investigate possible scaling factors to adapt the proposed relationship to other geometries as proposed by van Genuchten [1985]. Shrinking core models [Levenspiel, 1972] could also be explored as an alternative model to explain these experimental results.

Another limitation of the experiments and models developed in this paper derives from the use of hydrochloric acid and iron (III) chloride for preparing the leach solutions. The proposed in-situ process considers the use of sulphuric acid instead and generates iron (III) due to the action of iron-oxidizing microorganisms. This choice in the experimental design was made to lower the risk of clogging of the columns and pipes, as the presence of SO_4^{2-} ions might result in the precipitation of gypsum in contact to the dissolved calcium. As a result, the presented experiments and models could underestimate the precipitation of certain mineral phases such as gypsum that could be caused by dissolving calcium-bearing species in the presence of sulphate ions. The copper extraction rate might also be underestimated to some extent because only the couple Fe^{3+}/Fe^{2+} is at work in sulphate medium whereas the much stronger Cu^{2+}/Cu^{+} couple also participates in a chlorine medium.

Other parameters such as pressure and temperature are out of the scope of this study. Numerical simulations make it possible to adapt these parameters to in-situ conditions, e.g., adapting equilibrium with respect to temperature and pressure, but other possible effects such as the effect of temperature on the exchange rates should be addressed by combining experimental and modelling approaches. Additional experimental results would be required for properly controlling these aspects, but they are out of the scope of this paper.

Even if complementary experiments and models are thus necessary to confirm the applicability of the proposed models to indirect in-situ bioleaching, the presented results still provide interesting insights into the contribution of the diffusion within the porosity of rock particles. Namely, this study experimentally demonstrates an effect of the grain size on the leaching process, for which an interpretation in terms of diffusion within the grain porosity is proposed and numerically validated. A method is also proposed for extrapolating this model to in-situ conditions, which should be further tested and refined in future experimental and numerical studies. This study also points at several key factors for investigating in-situ leaching in similar contexts, in particular the role of atacamite and carbonates.

Atacamite ($Cu_2Cl(OH)_3$) is shown to yield a significant amount of copper during the acid leaching phase (up to 13 % of the available copper mass), but also brings additional chlorine in the solution and participates in the pH buffering. This study therefore advocates a better consideration of atacamite in further investigations on the applicability of indirect in-situ bioleaching to Kupferschiefer deposits or similar contexts where atacamite could be found.

The amount of carbonates among the mineral composition is shown to be another key factor in the applicability of the process. This parameter controls the efficiency of the acidification of the medium, but it has also been shown to produce a very sharp reaction front during the acid leaching phase, which requires a dramatical increase in the number of cells in the models for accurately reproducing this leaching phase. This effect has been observed to become more noticeable as the amount of carbonate increases, which implies that the leaching of these minerals could also cause dramatic modelling difficulties if present in too high quantity for future studies.

6 Conclusions

This paper presents a combined experimental and numerical modelling approach to investigate the processes involved in indirect in-situ bioleaching as proposed within the BIOMOre project [Filippov et al., 2017; Matthies et al., 2017]. Numerical simulations have proven very helpful in understanding the experimentally observed breakthrough curves. They have provided insight into the mineral dissolution sequences that occur inside the column and have made it possible to extrapolate the insights gained from the laboratory experiments to in-situ conditions.

The presented results suggest that a significant amount of copper can be recovered from the Zechstein mineralised sandstones through the proposed indirect in-situ bioleaching. The water-washing and acid leaching phases appear to efficiently remove part or all of the chlorine and carbonates under the conditions prevailing in the column experiments, depending on the geometrical properties of the porous medium.

The main contribution of this paper is derived from the modelling of the impact of the size of rock elements on the leaching process. Both experimental and numerical results suggest that, in this context, diffusion exerts a significant effect on the leaching reactions occurring throughout the grains, which effect is quantitatively evaluated with respect to grain size and compared to the effect of kinetics. The recovery curves presented in Fig. 4 indicate an increasing retardation effect as the size of the rock elements increases. The dual porosity models introduced in Section 3 are better able to reproduce the experimental results than equivalent single porosity models, which supports the conclusion about the impact of diffusion through the aqueous phase contained within the porosity of rock elements. Grain size appears to impact the kinetic rates, in particular for carbonates, and affects the removal of chlorine and carbonates. This impact further causes the retardation of copper extraction by extending the pH buffering effect of carbonates during the acid-ferric leaching phase.

In complement to the best fit models presented in Section 3, an exhaustive search of dual porosity parameters ($\%_{adv}$ and α) revealed a linear relationship between the logarithm of the exchange coefficient α and the logarithm of the ratio of diffusive and advective parts of the rock volume $\left(1-\%_{adv}\right)/\%_{adv}$. The intercept of the linear model is shown to linearly decrease with the increase of rock element size, which is in agreement with the observed increasing retardation with increasing grain size. From the mathematical relationship in Eq. (6), our dual porosity model is adapted to investigate in-situ recovery by considering a fracture corridor as an example of possible geometry. This model could be used as a basis for developing more complete scale-up schemes for in-situ conditions, in particular for bridging the gap between laboratory experiments and three-dimensional models at regional and reactor scales [Laurent et al., 2017].

The indirect in-situ bioleaching process, investigated by this study, represents a promising avenue for minimizing mining environmental impact and waste production. However, care should be taken to control possible environmental

impacts after decommissioning, which calls for both reliable stimulation techniques and physical means of maintaining well integrity during and after extraction. Exploitation sites should also be limited to those that do not pose any geological hazards. This study demonstrates that even a small amount of carbonate is able to rapidly inactivate the leach solutions, which can also be used as a safeguard for controlling the in-situ process.

This technology still represents a promising challenge and its application to new commodities and geological contexts needs to be further studied. Sullivan's prediction *"Eventually nearly every mine will be leached in place"* [Sullivan, 1931] has yet to become reality, but developing our understanding of fluid rock interactions would certainly be a key contributor towards the development of such alternative mining technologies.

Acknowledgements

The research leading to these results was supported by the European Union's Horizon 2020 research and innovation program under grant agreement No 642456 for the BIOMOre project. This publication reflects only the authors' view, exempting the Commission from any liability. Special thanks go to the KGHM company for providing the ore sample and to the BRGM for providing the thermodynamics and kinetic databases Thermoddem† for PhreeqC. Parts of this work have been carried out in the framework of the "Investissements d'avenir" Labex RESSOURCES21 (ANR-10-LABX-21).

Appendix A Mineral reconstruction procedure

The reconstruction of the mineralogical content of each grain size fraction from chemical element analysis is an important modelling stage because the numerical simulations have been observed to be quite sensitive to the abundance of certain minerals such as carbonate and atacamite. In this contribution, we consider a relatively complex set of minerals (Table 3) that approximates the mineral phases observed in the rock samples. To achieve this reconstruction, the chemical elements measured in each grain size fraction are progressively attributed to each mineral phase. First approximations are obtained by considering these measurements and observed ratios of certain minerals. For example, the mass of dolomite is estimated to be approximately twice the mass of calcite from Fourier Transform Infra-Red spectroscopy (FTIR). The repartition of copper in atacamite and the different sulphides is estimated from SEM images.

In a second stage, the observed experimental and numerical results are also incorporated in the process to reconcile the numerical results with the observed breakthrough curves. For example, we observed that the copper recovery reached a plateau during the acid leaching phase of the C2 experiments. This plateau is interpreted as the percentage of copper present in the atacamite minerals. While the plateau is not reached for the other experiments, it can be estimated by extrapolation of the recovery curves, and refined by comparing the numerical results with the observed recovery. Similar additional constraints were also derived for the percentage of remaining copper in anilite, and for the repartition of the various carbonates.

†http://thermoddem.brgm.fr/

The final step in the procedure starts by estimating the quantity of atacamite from the inferred percentage of copper leached during the acid leaching phase. The amount of thernadite is derived from the measured sulphate concentration. The remaining sodium is attributed to halite. The amount of microcline is derived from the potassium measurement. The remaining aluminium determines the amount of kaolinite, and the residual of silicon is interpreted as constituting quartz. The percentage of calcium attributed to ankerite is estimated based on mineral observations and numerical simulations. Magnesium measurements are used for estimating the amount of the remaining carbonate to be considered as dolomite, and the remaining calcium is finally attributed to calcite. A last empirical factor is used for determining the amount of remaining copper to be attributed to anilite and bornite respectively. The residual iron left by ankerite and bornite is finally attributed to pyrite.

The different empirical factors are optimised to ensure that the residual chemical elements are below one percent of the observed concentrations.

Appendix B Kinetics of dissolution reactions

This paper aims at describing the dissolution fronts that result from the complex interactions between the dissolution reactions of the different minerals (Table 7). The precipitation of minerals are disabled for simplifying the reactive system and because the experimental design does not aim at studying the possible precipitation and clogging effects. Most mineral dissolutions are treated by a kinetic approach, except for the thenardite. This anhydrous sodium sulphate mineral (Na_2SO_4) is treated by thermodynamics as it plays a minor role in the leaching process and is assumed to rapidly equilibrate with the leaching solution according to its solubility.

The kinetic rates are derived from recent additions to BRGM's Thermoddem† databases [Blanc et al., 2012; Kahnt et al., 2017; Marty et al., 2015]. They derive from the transition state theory after a formalism proposed by Lasaga et al. [1994]. For most of them, the dissolution rates $\mathcal{R}$ are computed as a product of various terms that account for the deviation from equilibrium, expressed by the term containing the ion activity product Q and equilibrium constant K, the available specific surface S (m^2/g), the decrease of available surface when the mineral dissolves, expressed as a ratio of the current and initial mass, respectively m and m_0 (g), and a term k that expresses the dependence to temperature and other possible catalytic or inhibitory effects ($\mathrm{mol}\cdot\mathrm{m}^2/\mathrm{s}$):

$$\mathcal{R} = m\,S\left(\frac{m}{m_0}\right)^{2/3} k\left(1-\frac{Q}{K}\right) \tag{8}$$

The term k gathers the effect of: (1) temperature, represented by the factor k_T, (2) pH, represented by $k_{\mathrm{H^+}}$ and $k_{\mathrm{OH^-}}$, and (3) the oxidative potential brought by iron (III), referred to as $k_{\mathrm{Fe^{3+}}}$. The various components of k are computed after Eq. (9), where $\mathrm{T_K}$ denotes the temperature in kelvin, R is the gas constant (8.314 $\mathrm{J}\cdot\mathrm{mol/K}$), and $[\cdot]$ refers to the activity of the given ion. The coefficients and exponents used in Eq. (9) are summarized in Table 8.

Table 8 Coefficients and exponents used in the computation of the factor k in kinetic rates. When a component is not used for a given mineral, its parameters are left empty and the corresponding of k_i is 1.

	S	k_T		k_{H^+}			k_{OH^-}			$k_{Fe^{3+}}$			
		a_T	b_T	a_{H^+}	$E_{a\,H^+}$	ν_{H^+}	a_{OH^-}	$E_{a\,OH^-}$	ν_{OH^-}	$a_{Fe^{3+}}$	$E_{a\,Fe^{3+}}$	$\nu_{Fe^{3+}}$	$\mu_{Fe^{3+}}$
Halite	1	12.21	7 400										
Calcite	0.7	2.564×10^{-2}	24 000	1.418×10^{2}	14 000	1.000							
Dolomite	0.09	2.615×10^{-3}	30 800	3.138×10^{4}	45 900	0.615							
Ankerite	0.09	2.615×10^{-3}	30 800	3.138×10^{4}	45 900	0.615							
Anilite	0.035	5.970×10^{2}	64 585	9.616×10^{5}	64 585	1.080				1.585×10^{9}	64 585	2.567	1.514
Bornite	0.039	1.175×10^{-5}	22 694	1.545×10^{-2}	22 694	0.832				4.603	22 694	0.836	0.789
Microcline	0.11	2.753×10^{-9}	31 000	4.508×10^{-6}	31 000	0.272	3.644×10^{-5}	31 000	0.354				
Kaolinite	11.8	6.119×10^{-8}	38 500	2.462×10^{-4}	42 900	0.513	2.458×10^{-3}	45 600	0.583				
Quartz	0.05	1.760	76 700				1.993×10^{4}	80 000	0.339				

$$k = k_T\ k_{H^+}\ k_{OH^-}\ k_{Fe^{3+}} \tag{9}$$
$$\text{with}\quad k_T = a_T\ \exp\left(-b_T/(\mathrm{R\,T_K})\right)$$
$$k_{H^+} = a_{H^+}\ \exp\left(-E_{a\,H^+}/(\mathrm{R\,T_K})\right)\ [H^+]^{\nu_{H^+}}$$
$$k_{OH^-} = a_{OH^-}\ \exp\left(-E_{a\,OH^-}/(\mathrm{R\,T_K})\right)\ [OH^-]^{\nu_{OH^-}}$$
$$k_{Fe^{3+}} = a_{Fe^{3+}}\ \exp\left(-E_{a\,Fe^{3+}}/(\mathrm{R\,T_K})\right)\ [H^+]^{\nu_{Fe^{3+}}}\ [Fe^{3+}]^{\mu_{Fe^{3+}}}$$

Atacamite is treated with a similar kinetic rate based on Eq. (8), with a S value of $3.191\ \mathrm{m^2/g}$ and with a different parameter k, adapted from [Le Roux et al., 2016]:

$$k = k_{atacamite}$$
$$\text{with}\quad \log_{10}(k_{atacamite}) = 1.64\ \log_{10}\left([H^+]\right) - 0.5 \tag{10}$$

Pyrite kinetic rate is computed after Eq. (8) with a parameter S of $0.05\ \mathrm{m^2/g}$ and k computed as:

$$k = k_1\ [H^+]^{-0.5}\ \sqrt{\frac{k_{Fe^3}\ [Fe(3)] + k_{O_2}\ [O_2]\ [H^+]^{0.14}}{k_{Fe^2}\ [Fe(2)] + k_{H^+}\ [H^+]^{-0.5}}} \tag{11}$$
$$\text{with}\quad k_1 = 1.715\times10^{6}\ \exp\left(-E_{a\,FeS_2}/(\mathrm{R\,T_K})\right)$$
$$k_{Fe^3} = 3.599\times10^{9}\ \exp\left(-E_{a\,Fe}/(\mathrm{R\,T_K})\right)$$
$$k_{Fe^2} = 9.419\times10^{-1}\ \exp\left(-E_{a\,FeS_2}/(\mathrm{R\,T_K})\right)$$
$$k_{H^+} = 3.310\times10^{12}\ \exp\left(-E_{a\,Fe}/(\mathrm{R\,T_K})\right)$$
$$k_{O_2} = 1.10\times10^{-3}$$
$$E_{a\,Fe} = 45\,000$$
$$E_{a\,FeS_2} = 79\,900$$

The kinetics for ankerite is derived from the dissolution rate of dolomite, as it is not present in the initial database. By comparison with the experimental results, it appeared necessary to apply a correction to the kinetic rates of carbonates, which have been adjusted by trial-and-error approach according to the factor summarised in Table 9. This is interpreted as a decrease of the reactive surface availability as the size of the sandstone grains increases.

Table 9 Factors applied to carbonate kinetic rates to account for the evolution of reactive surface with respect to grain size.

grain size fraction	Calcite	Dolomite	Ankerite
C2	1.0	1.0	0.8
C3	1.0	0.3	0.1
C4	1.0	0.15	0.05

References

Abhislash, B. D. Pandey, and A. K. Singh. Bioreactor leaching of uranium from a low grade indian ore. In *16th International Conference on Non-Ferrous Metals, New Delhi*, page 8, 2012. *(Cited page 4)*

S. K. Bhargava, R. Ram, M. Pownceby, S. Grocott, B. Ring, J. Tardio, and L. Jones. A review of acid leaching of uraninite. *Hydrometallurgy*, 151: 10–24, 2015. doi: 10.1016/j.hydromet.2014.10.015. *(Cited page 4)*

P. Blanc, A. Lassin, P. Piantone, M. Azaroual, N. Jacquemet, A. Fabbri, and E. C. Gaucher. Thermoddem: A geochemical database focused on low temperature water/rock interactions and waste materials. *Applied Geochemistry*, 27(10):2107–2116, 2012. doi: 10.1016/j.apgeochem.2012.06.002. *(Cited pages 3, 10, 11, and 19)*

S. C. Bouffard and D. G. Dixon. Investigative study into the hydrodynamics of heap leaching. *Metallurgical and Material Transaction*, 32(B):763–776, 2001. doi: 10.1007/s11663-001-0063-1. *(Cited page 3)*

M. L. Brusseau, R. E. Jessup, and P. S. C. Rao. Modeling the transport of solutes influenced by multiprocess non-equilibrium. *Water Resources Research*, 25:1971–1988, 1989. doi: 10.1029/WR025i009p01971. *(Cited page 8)*

W. H. Dresher. Producing copper nature's way: Bioleaching. *CWD: Innovations*, pages 1–10, 2004. *(Cited page 4)*

L. Filippov, C. Izart, H. Henjy, K. A. Hirsch, D. B. Johnson, R. Kahnt, H. Marten, and W. Slabbert. The BIOMOre project — a new mining concept for extracting metals from deep ore deposits using biotechnology. *Mining Report*, 153:436–445, 2017. *(Cited pages 2, 4, 6, and 18)*

D. M. Franks, R. Davis, A. J. Bebbington, S. H. Ali, D. Kemp, and M. Scurrah. Conflict translates environmental and social risk into business costs. *Proceedings of the National Academy of Sciences of the United States of America*, 111(21):7576–7581, 2014. doi: 10.1073/pnas.1405135111. *(Cited page 2)*

N. Habbache, N. Alane, S. Djerad, and L. Tifouti. Leaching of copper oxide with different acid solutions. *Chemical Engineering Journal*, 152: 503–508, 2009. *(Cited page 3)*

R. Haggerty and S. M. Gorelick. Multiple rate mass-transfer for modeling diffusion and surface reactions in media with pore-scale heterogeneity. *Water Resourceq Research*, 31:2383–2400, 1995. *(Cited page 11)*

J. Harrison and P. Arthur. The acidophilic thiobacilli and other acidophilic bacteria that share their habitat. *Annual Reviews in Microbiology*, 38(1): 265–292, 1984. *(Cited page 4)*

R. M. Izatt, S. R. Izatt, R. L. Bruening, N. E. Izatt, and B. A. Moyer. Challenges to achievement of metal sustainability in our high-tech society. *Chemical Society Reviews*, 43(8):2451–2475, 2014. doi: 10.1039/C3CS60440C. *(Cited page 2)*

R. Kahnt, M. Schlegel, P. Blanc, S. Guignot, and C. Izart. Overall systems model for bioleaching on local scale incorporating the results of the process of BRGM and CNRS together with the model parameter

database. Technical report, BIOMOre Deliverable 1.4, 2017. Accessed: 2019-04-19. *(Cited page 19)*

S. E. Kesler and A. C. Simon. *Mineral resources, economics and the environment*. Cambridge University Press, 2015. *(Cited page 2)*

K. Krupka, K. J. Cantrell, and B. P. McGrail. Thermodynamic data for geochemical modeling of carbonate reactions associated with CO2 sequestration – Literature Review . Technical report, Pacific Northwest National Lab. (PNNL), Richland, WA (United States), 2010. *(Cited page 11)*

H. Kucha and M. Pawlikowski. Two-brine model of the genesis of stratabound Zechstein deposits (Kupferschiefer type), Poland. *Mineralium Deposita*, 21:70–80, 1986. doi: 10.1007/BF00204365. *(Cited page 4)*

S. Kutschke, A. G. Guézennec, S. Hedrich, A. Schippers, G. Borg, A. Kamradt, J. Gouin, F. Giebner, S. Schopf, M. Schlömann, A. Rahfeld, J. Gutzmer, P. D´Hugues, K. Pollmann, S. Dirlich, and F. Bodénan. Bioleaching of Kupferschiefer blackshale–A review including perspectives of the Ecometals project. *Minerals Engineering*, 75:116–125, 2015. doi: 10.1016/j.mineng.2014.09.015. *(Cited pages 2 and 4)*

A. C. Lasaga, J. M. Soler, J. Ganor, T. E. Burch, and K. L. Nagy. Chemical weathering rate laws and global geochemical cycles. *Geochimica et Cosmochimica Acta*, 58(10):2361–2386, 1994. doi: 10.1016/0016-7037(94)90016-7. *(Cited page 19)*

G. Laurent, J.-J. Royer, F. Golfier, L. Filippov, Y. Gruzdeva, M. Vergnaud, C. Izart, and B. Lechenard. Geological model, deposit block model and reservoir model report. Technical report, BIOMOre Deliverable 2.2, 2017. Accessed: 2019-04-19. *(Cited page 18)*

S. G. Le Roux, J. A. Miller, A. J. Dunford, and C. E. Clarke. The dissolution kinetics of atacamite in the acid range and the stability of atacamite containing soils from Namaqualand, South Africa. *Applied Geochemistry*, 64:22–29, 2016. doi: 10.1016/j.apgeochem.2015.09.003. *(Cited page 20)*

O. Levenspiel. *Mineral resources, economics and the environment*. Wiley, New York, 1972. *(Cited page 18)*

D. G. Lundgren and M. Silver. Ore Leaching by Bacteria. *Annual Review of Microbiology*, 34(1):263–283, 1980. doi: 10.1146/annurev.mi.34.100180.001403. *(Cited page 4)*

E. Martens, H. Zhang, H. Prommer, J. Greskowiak, M. Jeffrey, and P. Roberts. In situ recovery of gold: Column leaching experiments and reactive transport modeling. *Hydrometallurgy*, 125–126:16–23, 2012. doi: 10.1016/j.hydromet.2012.05.005. *(Cited page 4)*

N. C. M. Marty, F. Claret, A. Lassin, J. Tremosa, P. Blanc, B. Madé, E. Giffaut, B. Cochepin, and C. Tournassat. A database of dissolution and precipitation rates for clay-rocks minerals. *Applied Geochemistry*, 55:108–118, 2015. doi: 10.1016/j.apgeochem.2014.10.012. *(Cited page 19)*

R. Matthies, H. Hejny, K. Hirsch, R. Kahnt, H. Märten, and D. B. Johnson. In-situ bioextraction of industry metals from deep ore deposits to secure EU resource supply. *GeoResources Journal*, 2:37–40, 2017. *(Cited pages 2, 4, 6, and 18)*

K. Moffat and A. Zhang. The paths to social licence to operate: An integrative model explaining community acceptance of mining. *Resources Policy*, 39(1):61–70, 2014. doi: 10.1016/j.resourpol.2013.11.003. *(Cited page 2)*

R. L. Moss, E. Tzimas, H. Kara, P. Willis, and J. Kooroshy. *Critical Metals in Strategic Energy Technologies: Assessing Rare Metals as Supply-Chain Bottlenecks in Low-Carbon Energy Technologies*. Luxembourg: Publications Office of the European Union, 2011. doi: 10.2790/35600. *(Cited page 2)*

S. Oszczepalski. Origin of the Kupferschiefer polymetallic mineralization in Poland. *Mineralium deposita*, 34:599–613, 1999. *(Cited page 4)*

E. Pakostova, B. M. Grail, and D. B. Johnson. Bio-processing of a saline, calcareous copper sulfide ore by sequential leaching. *Hydrometallurgy*, 179:36–43, 2018. doi: 10.1016/j.hydromet.2018.05.004. *(Cited pages 3, 4, and 6)*

D. L. Parkhurst and C. A. J. Appelo. User's guide to PHREEQC (Version 2)–A computer program for speciation, batch-reaction, one-dimensional transport, and inverse geochemical calculations. In *Water-Resources Investigations Report 99-4259*, page 312. U.S. Geological Survey, 1999. *(Cited pages 8, 9, 11, and 15)*

D. L. Parkhurst and C. A. J. Appelo. Description of input and examples for PHREEQC version 3–A computer program for speciation, batch-reaction, one-dimensional transport, and inverse geochemical calculations. In *Techniques and Methods*, volume 6, chapter A43, page 497. U.S. Geological Survey, 2013. *(Cited pages 8 and 15)*

J. Petersen. Modelling of bioleach processes: Connection between science and engineering. *Hydrometallurgy*, 104(3–4):404–409, 2010. doi: 10.1016/j.hydromet.2010.02.023. *(Cited page 3)*

J. Petrie. New Models of Sustainability for the Resources Sector. *Process Safety and Environmental Protection*, 85(1):88–98, 2007. doi: 10.1205/psep.05179. *(Cited page 2)*

W. J. Rankin. *Minerals, Metals and Sustainability: Meeting Future Material Needs*. CSIRO publishing, 2011. *(Cited page 2)*

D. E. Rawlings. Heavy metal mining using microbes. *Annual Reviews in Microbiology*, 56(1):65–91, 2002. doi: 10.1146/annurev.micro.56.012302.161052. *(Cited pages 2, 3, and 4)*

D. E. Rawlings and D. B. Johnson. The microbiology of biomining: Development and optimization of mineral-oxidizing microbial consortia. *Microbiology*, 153(2):315–324, 2007. doi: 10.1099/mic.0.2006/001206-0. *(Cited pages 2, 3, and 4)*

D. E. Rawlings and S. Silver. Mining with Microbes. *Nature Biotechnology*, 13(8):773–778, 1995. doi: 10.1038/nbt0895-773. *(Cited page 4)*

M. Riekkola-Vanhanen. Talvivaara mining company – From a project to a mine. *Minerals Engineering*, 48:2–9, 2013. doi: 10.1016/j.mineng.2013.04.018. *(Cited page 4)*

T. Rohwerder, T. Gehrke, K. Kinzler, and W. Sand. Bioleaching review part a:. *Applied Microbiology and Biotechnology*, 63(3):239–248, 2003. doi: 10.1007/s00253-003-1448-7. *(Cited page 4)*

M. Seredkin, A. Zabolotsky, and G. Jeffress. In situ recovery, an alternative to conventional methods of mining: Exploration, resource estimation, environmental issues, project evaluation and economics. *Ore Geology Reviews*, 79:500–514, 2016. doi: 10.1016/j.oregeorev.2016.06.016. *(Cited pages 2, 3, and 4)*

L. Sinclair and J. Thompson. In situ leaching of copper: Challenges and future prospects. *Hydrometallurgy*, 157:306–324, 2015. doi: 10.1016/j.hydromet.2015.08.022. *(Cited page 2)*

C. I. Steefel and K. Maher. Fluid-rock interaction: A reactive transport approach. *Reviews in mineralogy and geochemistry*, 70(1):485–532, 2009. doi: 10.2138/rmg.2009.70.11. *(Cited page 3)*

C. I. Steefel, D. J. DePaolo, and P. C. Lichtner. Reactive transport modeling: An essential tool and a new research approach for the Earth sciences. *Earth and Planetary Science Letters*, 240(3):539–558, 2005. doi: 10.1016/j.epsl.2005.09.017. *(Cited page 3)*

C. I. Steefel, C. A. J. Appelo, B. Arora, D. Jacques, T. Kalbacher, O. Kolditz, V. Lagneau, P. C. Lichtner, K. U. Mayer, J. C. Meeussen, S. Molins, D. Moulton, H. Shao, J. Šimunek, N. Spycher, S. B. Yabusaki, and G. T. Yeh. Reactive transport codes for subsurface environmental simulation. *Computational Geosciences*, 19(3):445–478, 2015. doi: 10.1007/s10596-014-9443-x. *(Cited page 3)*

J. D. Sullivan. Leaching Copper From Its Ores. *Journal of Chemical Education*, 8(5):829–847, 1931. doi: 10.1021/ed008p829. *(Cited pages 3, 4, and 19)*

H. Tributsch. Direct versus indirect bioleaching. *Hydrometallurgy*, 59:177–185, 2001. doi: 10.1016/S0304-386X(00)00181-X. *(Cited page 4)*

M. T. van Genuchten. A general approach for modeling solute transport in structured soils. Technical report, International Association of Hydrogeologists Memoirs, 1985. *(Cited pages 10 and 18)*

P. J. Van Staden and J. Petersen. First-order exchange and spherical diffusion models of heap leaching in PhreeqC. *Journal of the Southern African Institute of Mining and Metallurgy*, 118(7):681–694, 2018. doi: 10.17159/2411-9717/2018/v118n7a2. *(Cited page 11)*

S. Wang. Copper leaching from chalcopyrite concentrates. *The journal of the minerals*, pages 48–51, 2005. doi: 10.1007/s11837-005-0252-5. *(Cited page 4)*